Fakultät für Physik
Institut für Theoretische Festkörperphysik

# Influence of strong noise on the Adiabatic Quantum Computer

## Der Einfluss von starkem Rauschen auf den Adiabatischen Quanten Computer

Diploma Thesis

by

Philipp Rudo

January 7, 2015

Instructor: Prof. Dr. Gerd Schön
2nd Instructor: Prof. Dr. Matthias Troyer
Advisor: Dr. Michael Marthaler

Hiermit erkläre ich, dass ich die vorliegende Diplomarbeit selbständig verfasst und gelieferte Datensätze und graphische Darstellungen selbständig erstellt habe. Ich habe keine anderen Quellen als die angegebenen benutzt und habe die Stellen der Arbeit, die anderen Werken entnommen sind in jedem einzelnen Fall unter Angabe der Quelle als Entlehnung kenntlich gemacht.

Philipp Rudo
Karlsruhe, den 07.01.2015

# Contents

# Chapter 1

# 1 Introduction

Classical computers quickly reach their limits when it comes to quantum mechanical or other problems with an exponentially growing complexity. To overcome this limit, Richard Feynman proposed in 1982 to map computational problems on the eigenstates of quantum mechanical systems, rather than classical states [1]. Today this idea is known as quantum computation. By that the computational state is not only given by one sequence of the two computational states 0 and 1, but by the superposition of any such sequences. Thus it is possible to not only try each possible result one by one but all in parallel, gaining a exponential speed up in such problems is expected. While in the beginning the focus was placed on solving quantum mechanical problems, as they obey the same rules as the computational states, Peter Shor proved with his factorization algorithm that the principle of quantum computing can also be used to speed up other mathematical problems [2].

In 2001 Farhi et al. proposed a new idea how quantum computation can be realized [3]. Instead of using gates, elementary operations on the qubits, as Feynman suggested, they proposed to use the adiabatic theorem for computation. Thereby the state is prepared in the ground state of a simple Hamiltonian and then adiabatically transferred to a problem Hamiltonian in which the computational problem is encoded. By the adiabatic transition, the state of the quantum computer stays in the ground state throughout the transition such that the correct solution can directly be measured after the transition is completed. While this method naturally is ideal for optimization problems the group of Aharonov et al. showed in 2007 that the concept of the adiabatic quantum computer is, in principle, capable of computing general problems [4].

However, both methods have a problem when it comes to a practical implementation. By the quantum mechanical nature of the computational state, the quantum computer becomes extremely sensitive to uncontrollable interactions with the environment. While for the universal quantum computer, based on gates, there are ideas how to correct errors occurring from such interactions [5], there is no accepted theory describing the adiabatic quantum computer. Furthermore it is unclear if the adiabatic quantum computer can obtain a speed up compared to classical computers. For the adiabatic theorem to hold, the duration of the transition must be much larger than the inverse of the minimal gap between the ground and first excited state. But, in 2010 Altshuler et al. showed that for the Exact Cover 3 algorithm and one specific adiabatic transition the minimal gap closes exponentially at the end of the transition [6]. Thus, in this case the computation time needed to solve the problem grows exponentially, like for classical computers. Although this does not exclude a possible speed up, as for other problems or adiabatic transitions the gap might behave differently, it shows that detecting the speed up is complicated, as it depends on the specific implementation of the quantum algorithm.

Despite of the problems in implementation, the Canadian company D-Wave announced in 2004 their plan to build a quantum computer, based on the concept of the adiabatic quantum computer, and claims that this concept is naturally robust against environmental influences [7]. Six years after the announcement D-Wave presented in 2010 the D-Wave One, the self-claimed first commercially available quantum computer, build up of 128 superconducting flux qubits. In spite of all the marketing claims D-Wave makes, the skepticism about the functionality and reliability of the device never died. Up until today there is no explicit proof whether the D-Wave One is fundamentally quantum or merely performs a calculation equivalent to that of a classical stochastic computer.

We structure the work the following way:

First, we provide in Chap. 2 the necessary background information how the D-Wave One is build up, summarize the current discussion about the device and review the articles this work is based on. In Chap. 3 we derive our model for the adiabatic quantum computer in the presence of noise. The model is microscopically motivated, where all necessary parameters can be taken from experiments. Furthermore we investigate the dynamics in lowest-order perturbation theory following from our model for a single and two coupled qubits. After that, we apply in Chap. 4 the model in a simulation to a system of 108 qubits with 1000 random sets of couplings to find the success probability in finding the ground state. Finally, we summarize in Chap. 5 the results from this thesis and shortly discuss the next steps to gain further insight about the model.

# Chapter 2
# 2 Background

*In this chapter we present an overview of the background information the later work is based on. First, we introduce in Sec. 2.1 the idea behind the adiabatic quantum computer in more detail. Then, we present in Sec. 2.2 the basic functionality of the superconducting flux qubits and the structure if the chip used in the D-Wave One. After that, we report in Sec. 2.3 on a model for macroscopic flux tunneling in a single superconducting flux qubit and the corresponding experiment performed on the CCJJ rf-SQUID used in the device. Both, the predictions of the model and data gained from the experiment are in agreement. Finally we review in Sec. 2.4 the latest discussion about the D-Wave One, where we concentrate on the part needed for this work.*

## 2.1 The Adiabatic Quantum Computer

### 2.1.1 The Adiabatic Theorem

The Adiabatic Theorem follows from the study of slowly evolving quantum-systems over time. It states, that for slowly varying Hamiltonians the instantaneous eigenstates will evolve continuously into the corresponding instantaneous eigenstates at a later time. Where the difference between the initial and final Hamiltonian can be huge, such that it cannot be treated perturbatively.

To derive the adiabatic theorem, let us consider a Hamiltonian $\mathcal{H}(\boldsymbol{\chi}(t))$ that interacts with the environment via a set of time-dependent, classical parameters $\boldsymbol{\chi}(t) = (\chi_1(t), \chi_2(t), \dots)$. Let us further assume that the parameters $\boldsymbol{\chi}(t)$ are slowly varying, smooth functions in time and that the Hamiltonian $\mathcal{H}(\boldsymbol{\chi}(t))$ has a discrete and non-degenerate spectrum. From the fact that the parameters $\boldsymbol{\chi}(t)$ are smooth follows that also the Hamiltonian must be smooth, meaning that its eigenstates and eigenvalues are smooth functions in time. In the future we denote $\mathcal{H}(\boldsymbol{\chi}(t)) \equiv \mathcal{H}(t)$ for convenience. At any time we can find an instantaneous eigenbasis with

$$\mathcal{H}(t)\,|n(t)\rangle = E_n(t)\,|n(t)\rangle \quad \text{and} \quad \langle m(t)|n(t)\rangle = \delta_{mn} \tag{2.1}$$

where the index $n$ represents a set of quantum numbers that determines the eigenstate. Without loss of generality we can assume that $E_0(t) < E_1(t) < \dots$ . Thereby the solution of the time-dependent Schrödinger equation, using $\hbar = 1$,

$$\mathrm{i}\partial_t\,|\Psi(t)\rangle = \mathcal{H}(t)\,|\Psi(t)\rangle \tag{2.2}$$

is given by a linear combination of the eigenstates

$$|\Psi(t)\rangle = \sum_n c_n(t) \mathrm{e}^{\mathrm{i}\theta_n(t)} |n(t)\rangle \ , \tag{2.3}$$

where

$$\theta_n(t) = -\int_0^t \mathrm{d}t' \ E_n(t') \tag{2.4}$$

is the generalized dynamic phase for time-dependent eigenvalues.

Inserting the ansatz Eq. (2.3) into the Schrödinger equation Eq. (2.2) leads to

$$\mathrm{i}\partial_t |\Psi\rangle = \mathrm{i}\sum_n \left(\dot{c}_n |n\rangle + c_n |\dot{n}\rangle + \mathrm{i}c_n\dot{\theta}_n |n\rangle\right) \mathrm{e}^{\mathrm{i}\theta_n} \stackrel{!}{=} \sum_n c_n \underbrace{\mathcal{H}|n\rangle}_{-\dot{\theta}_n|n\rangle} \mathrm{e}^{\mathrm{i}\theta_n} \ , \tag{2.5}$$

where the dot denotes time derivation and the time argument has been omitted (and will be in future) for a better readability. From Eq. (2.4) it is easy to see that $E_n = -\dot{\theta}_n$ and thus the last term on the LHS cancels the RHS. With this and after taking the inner product with a second eigenstate $|m\rangle$ follows

$$\dot{c}_m = -\sum_n c_n \langle m|\dot{n}\rangle \, \mathrm{e}^{\mathrm{i}(\theta_n - \theta_m)} \ , \tag{2.6}$$

which is a set of coupled differential equation for the coefficients $c_m$.

In Eq. (2.6) the matrix element $\langle m|\dot{n}\rangle$ is still unknown. We can find an expression for it by taking the time derivation of Eq. (2.1), leading to

$$\dot{\mathcal{H}}|n\rangle + \mathcal{H}|\dot{n}\rangle = \dot{E}_n|n\rangle + E_n|\dot{n}\rangle \ , \tag{2.7}$$

and taking the inner product with eigenstate $|m\rangle$

$$\langle m|\dot{\mathcal{H}}|n\rangle + \underbrace{\langle m|\mathcal{H}|\dot{n}\rangle}_{E_m\langle m|\dot{n}\rangle} = E_n\langle m|\dot{n}\rangle + \dot{E}_n\langle m|n\rangle \ . \tag{2.8}$$

For $m \neq n$ this can be solved for $\langle m|\dot{n}\rangle$, leading to

$$\langle m|\dot{n}\rangle = \frac{\langle m|\dot{\mathcal{H}}|n\rangle}{E_n - E_m} \, . \tag{2.9}$$

Substituting Eq. (2.9) into Eq. (2.6) we finally get the coupled differential equation

$$\dot{c}_m = -c_m\langle m|\dot{m}\rangle - \sum_{n\neq m} c_n \frac{\langle m|\dot{\mathcal{H}}|n\rangle}{E_n - E_m} \mathrm{e}^{\mathrm{i}(\theta_n - \theta_m)} \tag{2.10}$$

for the coefficients $c_m$.

When we now assume that the system was initiated in state $|m\rangle$, then the first term gives the probability for the system to stay in state $|m\rangle$ while the second term gives the probability for the system to jump to an other state $|n\rangle$. Note that up to this point the derivation is exact. At this point we now make the adiabatic approximation by neglecting the second term in Eq. (2.10). This

approximation is justified, as we assume that the parameters $\boldsymbol{\chi}(t)$, and thus the Hamiltonian $\mathcal{H}$, only changes very slowly in time which leads to $\langle m|\dot{\mathcal{H}}|n\rangle \approx 0$.

By using the adiabatic approximation the differential equations for the coefficients $c_m$, Eq. (2.10), become decoupled, leading to

$$\dot{c}_m = -c_m \langle m|\dot{m}\rangle \,, \tag{2.11}$$

which can directly be solved to

$$c_m(t) = c_m(0)\mathrm{e}^{-i\gamma_m(t)} \,, \tag{2.12}$$

where

$$\gamma_m(t) = i\int_0^t \mathrm{d}t' \ \langle m|\dot{m}\rangle \,. \tag{2.13}$$

is the geometric phase. It is worth to mention that by its definition the geometric phase $\gamma_m$ is completely real as

$$\frac{\mathrm{d}}{\mathrm{d}t}\langle m|m\rangle = \langle \dot{m}|m\rangle + \langle m|\dot{m}\rangle = 2\,\mathrm{Re}\,\langle m|\dot{m}\rangle \stackrel{!}{=} \frac{\mathrm{d}}{\mathrm{d}t}1 = 0\,. \tag{2.14}$$

Hence the states of the system gain an additional phase factor, as implied by the name geometric phase, by the adiabatic evolution.

### 2.1.2 The Adiabatic Quantum Computer & Quantum Annealer

The Adiabatic Quantum Computer is a quantum optimization algorithm that is based on the adiabatic evolution of a quantum system [8]. The idea behind it is pretty simple. Let us assume we have a problem described by Hamiltonian $\mathcal{H}_\mathrm{P}$. In general calculating the ground state of $\mathcal{H}_\mathrm{P}$, analytically or numerically on classical computers, is extremely hard if at all possible. To perform adiabatic quantum computation we then take a simple starting Hamiltonian $\mathcal{H}_0$, prepare its ground state and adiabatically transfer it to the problem Hamiltonian $\mathcal{H}_\mathrm{P}$. As shown in Sec. 2.1.1, the adiabatic theorem ensures, if the transition is performed slow enough, that the system will always stay in its instantaneous ground state. Thus, after the transition the state of the adiabatic quantum computer is given by the ground state of the problem Hamiltonian $\mathcal{H}_\mathrm{P}$ and can directly be measured. In principle this method is capable of solving any mathematical problem that can be solved by an universal quantum computer based on gates [4].

More formally, the adiabatic quantum computer is described by the Hamiltonian

$$\mathcal{H} = \mathrm{A}(t)\mathcal{H}_0 + \mathrm{B}(t)\mathcal{H}_\mathrm{P} \tag{2.15}$$

where $\mathrm{A}(t)$ and $\mathrm{B}(t)$ are classical parameters denoted as $\boldsymbol{\chi}(t)$ in Sec. 2.1.1. We choose the parameters in such a way that $\mathrm{A}(0) \gg \mathrm{B}(0)$ and $\mathrm{A}(t_f) \ll \mathrm{B}(t_f)$, where $t_f$ denotes the time at the end of the transition. For simplicity, let us assume that $\mathrm{A}(t)$ and $\mathrm{B}(t)$ are linear and run from 0 to 1 or vice versa, i. e. that the Hamiltonian is given by

$$\mathcal{H} = \left(1 - \frac{t}{t_f}\right)\mathcal{H}_0 + \frac{t}{t_f}\mathcal{H}_\mathrm{P} \,. \tag{2.16}$$

The crucial point for the implementation of the adiabatic quantum computer is, how large $t_f$ has to be chosen such that the adiabatic theorem still holds.

We can estimate $t_f$ by using the second term of Eq. (2.10), which gives the probability of the system to change its state. Because we initiate the state in the ground state of the starting Hamiltonian $\mathcal{H}_0$, the initial conditions for the coefficients $c_m$ are given by

$$c_m(0) = \begin{cases} 1 & \text{for } m = 0 \\ 0 & \text{for } m \neq 0 \end{cases} . \tag{2.17}$$

From the initial condition also follows, that the time derivative of the coefficients, for $m \neq 0$, and thus the probability for the excited states to be populated, is

$$\dot{c}_m \propto \frac{1}{E_0 - E_m} . \tag{2.18}$$

Thus it is sufficient to concentrate on the transition between the ground and the first excited state, as they are most likely to occur. When we substitute Eq. (2.16) into Eq. (2.10) and further assume that the eigenvalues are time-independent, and thus $\theta_n = E_n t$, we get

$$\dot{c}_1 = \frac{\langle 0|\dot{\mathcal{H}}|1\rangle}{E_0 - E_1} \mathrm{e}^{\mathrm{i}(E_0 - E_1)t} = \frac{1}{t_f} \frac{\langle 0| - \mathcal{H}_0 + \mathcal{H}_\mathrm{P}|1\rangle}{E_0 - E_1} \mathrm{e}^{\mathrm{i}(E_0 - E_1)t} , \tag{2.19}$$

which can be directly integrated leading to

$$c_1 \propto \frac{1}{t_f} \frac{\langle 0| - \mathcal{H}_0 + \mathcal{H}_\mathrm{P}|1\rangle}{(E_0 - E_1)^2} . \tag{2.20}$$

As a result we can now define an upper bound $\bar{c}_1$ for the system to leave the ground state, given by

$$\bar{c}_1 \propto \frac{1}{t_f \Delta_\mathrm{min}} \frac{\mathcal{E}}{\Delta_\mathrm{min}} , \tag{2.21}$$

where $\mathcal{E} = \max\limits_{0 \leq t \leq t_f} \langle 0| - \mathcal{H}_0 + \mathcal{H}_\mathrm{P}|1\rangle$ is the maximal overlap and $\Delta_\mathrm{min} = \min\limits_{0 \leq t \leq t_f} |E_0 - E_1|$ the minimal gap between the ground state and the first excited state. For typical physical systems the maximal overlap and the minimal gap are of the same order of magnitude, $\mathcal{O}(\mathcal{E}) = \mathcal{O}(\Delta_\mathrm{min})$, and thus $\mathcal{E}/\Delta_\mathrm{min} \approx 1$. From this follows that the transition can be assumed to be adiabatically when

$$\bar{c}_1 = \frac{1}{t_f \Delta_\mathrm{min}} \ll 1 \tag{2.22}$$

or equivalent, when

$$t_f \gg \frac{1}{\Delta_\mathrm{min}} . \tag{2.23}$$

This result directly gives an account to the fact that there are different energy scales in the system. By the adiabatic transition the energy of the system is not conserved but changes with

$$\omega_0 \propto \frac{1}{t_f} . \tag{2.24}$$

Using Eq. (2.24) the condition for the adiabatic theorem to hold, Eq. (2.23), can be written as

$$\omega_0 \ll \Delta_\mathrm{min} . \tag{2.25}$$

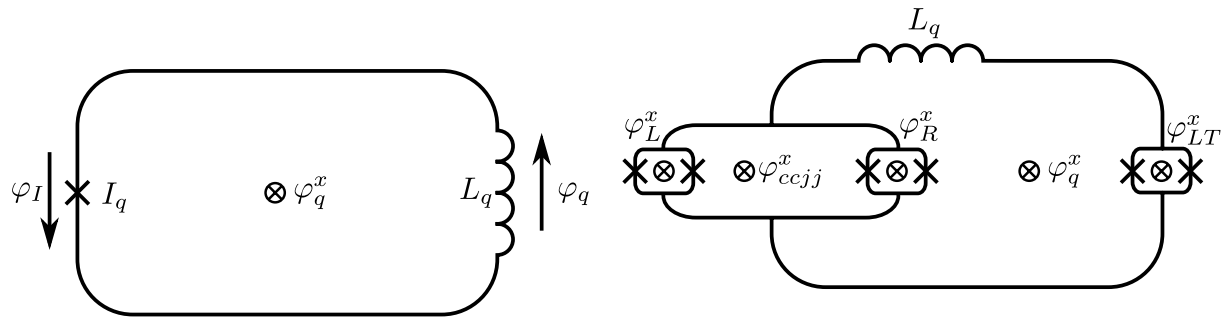


**(a)** **(b)**

**Figure 2.1:** Sketch of (a) a simple rf-SQUID and (b) a CCJJ rf-SQUID, used in the D-Wave One. Critical currents at the Josephson junction are denoted $I_i$ and the corresponding phases $\varphi_i$. The inductance of the superconducting loop is given by $L_q$. For the CCJJ rf-SQUID this is a effective quantity given by the inductance of the main and the CCJJ loop. Parameters of the qubit can be controlled by external fluxes represented by the phases $\varphi_i^x$.

From this follows that the adiabatic theorem holds once the energy scale given by the adiabatic transition is much smaller than the energy scale given by the spectrum of the system.

Although the D-Wave One implements the algorithm of the adiabatic quantum computer, D-Wave uses the term quantum annealer, instead of adiabatic quantum computer, for their device. This is because in the discussion above we omitted any coupling to the environment, besides the parameters $\mathrm{A}(t)$ and $\mathrm{B}(t)$ which were assumed to be perfect. In reality however, there is always noise disturbing the adiabatic quantum computer. In the case of the D-Wave One this noise is very strong, which leads to coherence times of the order of $\mathcal{O}(\,\mathrm{ns}) \ll \mathcal{O}(\,\mu\mathrm{s})$ the length of the transition. Thus, there is no entanglement of the states, which is needed for the adiabatic quantum computer, throughout the transition in the D-Wave One. Nevertheless D-Wave states that their device is naturally robust against coupling to the environment and decided, to avoid confusion, to call it a quantum annealer.

## 2.2 The D-Wave One

The "Processor" of the D-Wave One is a chip containing CCJJ rf-SQUID qubits. In this section we shortly review the most important properties of the chip. For a full discussion see [9] and the citations within.

The simplest realization of an flux qubit is the rf-SQUID shown in Fig. 2.1a and is made up by a superconducting loop with one Josephson junction in it. In this case the phase across the junction is the same as the phase change across the loop, i. e. $\varphi_I = \varphi_q$. Thus its Hamiltonian can be written as

$$\mathcal{H} = \frac{Q_q^2}{2C_q} + V(\varphi_q) \tag{2.26a}$$

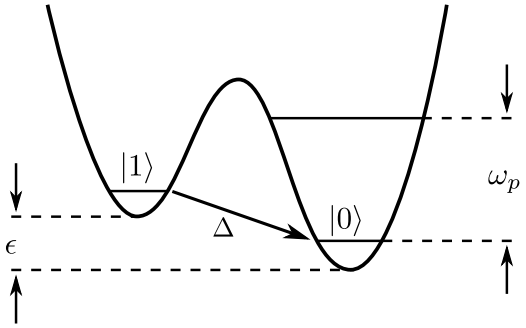


**Figure 2.2:** Sketch of a typical double-well potential found in flux qubits. Between the states with the lowest energy in both wells is a energy splitting $\epsilon$. The energy difference between the lowest and first excited states inside each well is of the order of the plasma frequency $\omega_p$. In the case when $\epsilon \ll \omega_p$ only tunneling between the lowest states of the two wells, with the tunneling amplitude $\Delta$, have to be considered.

where the potential is given by

$$V(\varphi_q) = U_q \left[ \frac{1}{2}(\varphi_q - \varphi_q^x)^2 - \beta \cos(\varphi_q) \right] \tag{2.26b}$$

with

$$\beta = \frac{2\pi L_q I_q}{\Phi_0} \,. \tag{2.26c}$$

Here $Q_q$ is the charge, $C_q$ the capacitance, $L_q$ the inductance and $I_q$ the critical current of the qubit. Furthermore the phase of the qubit is given by $\varphi_q$, an externally applied phase, by applying an external flux, by $\varphi_q^x$ and the flux quantum by $\Phi_0$.

If now the qubit is designed the way such that $\beta > 1$ and the external flux is tuned such that $\varphi_q^x \approx \pi$ the potential energy $V(\varphi_q)$ forms a double well potential, as shown in Fig. 2.2, where the potential barrier increases with increasing $\beta$. Inside each of the wells the lowest states are separated to the excited states by an energy of the order of the rf-SQUID plasma frequency $\omega_p = 1/\sqrt{L_q C_q}$. Thus if the energy of the qubit is $\ll \omega_p$ only the lowest states in both well can be occupied. In this regime the Hamiltonian Eq. (2.26a) can be approximated by

$$\mathcal{H}_q = -\frac{1}{2}(\epsilon \sigma_z + \Delta \sigma_x) \tag{2.27}$$

where $\epsilon$ is the energy splitting and $\Delta$ the tunneling amplitude through the potential barrier between both states. Hereby both, $\epsilon$ and $\Delta$, are functions of the intrinsic parameters of the qubit, e. g. the inductance $L_q$ or the critical current $I_q$.

This dependency of the intrinsic parameters makes it impractical to build large-scale devices from rf-SQUID qubits as the intrinsic parameters and with this the properties of the qubit are fixed at fabrication. But from this also follows that the properties of the qubit are sensitive to small variations during fabrication. Thus it is nearly impossible to fabricate a large-scale chip, that has rf-SQUID qubits with identical properties. Furthermore, implementation of an AQC requires the ability to tune

the tunneling amplitude $\Delta$ from being the dominant term in Eq. (2.26a) to be negligible small during the computation. But this is not possible for an rf-SQUID qubit. Thus the practical use of such a rf-SQUID qubit is limited.

To overcome the problems at fabrication the compound-compound Josephson junction (CCJJ) rf-SQUID flux qubit, as shown in Fig. 2.1b, was developed. When we compare the two designs we see that the single Josephson junction in the rf-SQUID was replaced by an CCJJ-loop, containing a major loop and two minor ones, denoted as left ($L$) and right ($R$) loop, with two Josephson junction each. With this now the critical current $I_q$, fixed by the properties of the Josephson junction in the rf-SQUID, is now determined by the properties of the CCJJ-loop and thus becomes tuneable with the external phases $\varphi_L^x$ and $\varphi_R^x$, i. e.

$$I_q = I_L \cos\frac{\varphi_L^x}{2} + I_R \cos\frac{\varphi_R^x}{2} \tag{2.28}$$

where $I_{L,R} = I_{L,R}^1 + I_{L,R}^2$ is the sum of the critical currents of the Josephson junctions in the left and right loop respectively. In addition to the CCJJ-loop the CCJJ rf-SQUID also contains a new small loop with two Josephson junctions, called an inductance tuner ($L$ tuner). Therefore the loop is designed the way that $I_{LT}\cos\varphi_{LT}^x/2 \gg I_q$, where $I_{LT}$ is the net critical current of the loop and $\varphi_{LT}^x$ an external phase applied to the loop. In this regime the phase change at the $L$ tuner can be neglected. If one additionally assumes that the inductance of the $L$ tuner wiring itself can be neglected then the overall inductance of the qubit is given by

$$L_q = L_q^0 + \frac{\Phi_0}{2\pi I_{LT}\cos\varphi_{LT}^x/2} \tag{2.29}$$

where $L_q^0$ is the intrinsic inductance of the qubit.

Using the changes discussed above the overall complexity of the circuit grows and fabrication becomes more difficult. But at the same time we gain more control, by applying external magnetic fluxes, over the qubit. As shown in Eq. (2.28) now the critical current of the qubit can be controlled via the two static phases $\varphi_L^x$ and $\varphi_R^x$. Hereby the phase $\varphi_R^x$ is chosen and then $\varphi_L^x$ is adjusted to compensate the variation from fabrication and thus balance the value of the critical current for multiple qubits. For the inductance $L_q$ the same can be done via the static phase $\varphi_{LT}^x$. Doing so the energy splitting $\epsilon$ and tunneling amplitude $\Delta$ become basically functions of the two phases $\varphi_q^x$ and $\varphi_{ccjj}^x$. Thus, by choosing $\varphi_q^x$ and $\varphi_{ccjj}^x$ to be time-dependent, they can be used to implement the annealing schedule needed for the implementation of the AQC.

Knowing how the qubits work let us now have a look at the layout of the chip used in the D-Wave One. The chip is made up of several unit cells each containing 8 qubits. Inside one of those unit cells there are four qubits aligned horizontally and four vertically. The qubits couple pairwise to each other. Whereby the horizontally aligned qubits couple to all of the vertically aligned ones and the other way round. Fig. 2.3 shows a sketch of one of the unit cells. The chip then contains a grid of $4 \times 4$ of those unit cells. The unit cells are coupled to each other by coupling each qubit to the corresponding qubit of the neighboring unit cells, e. g. in Fig. 2.3 $q_0$ is coupled to the corresponding $q_0$'s of the unit cell above and below the shown one.

This structure dictates the way the qubits can couple with each other, which has influence on the implementation of the simulation later on. From the structure of the chip follows directly that each qubit can be coupled to a maximum of 6 other qubits, e. g. $q_0$ can couple to the four horizontally aligned qubits plus the corresponding two qubits from the unit cell above and below. Furthermore when two qubits couple to each other then any qubit coupled to one of those two qubits cannot couple to the

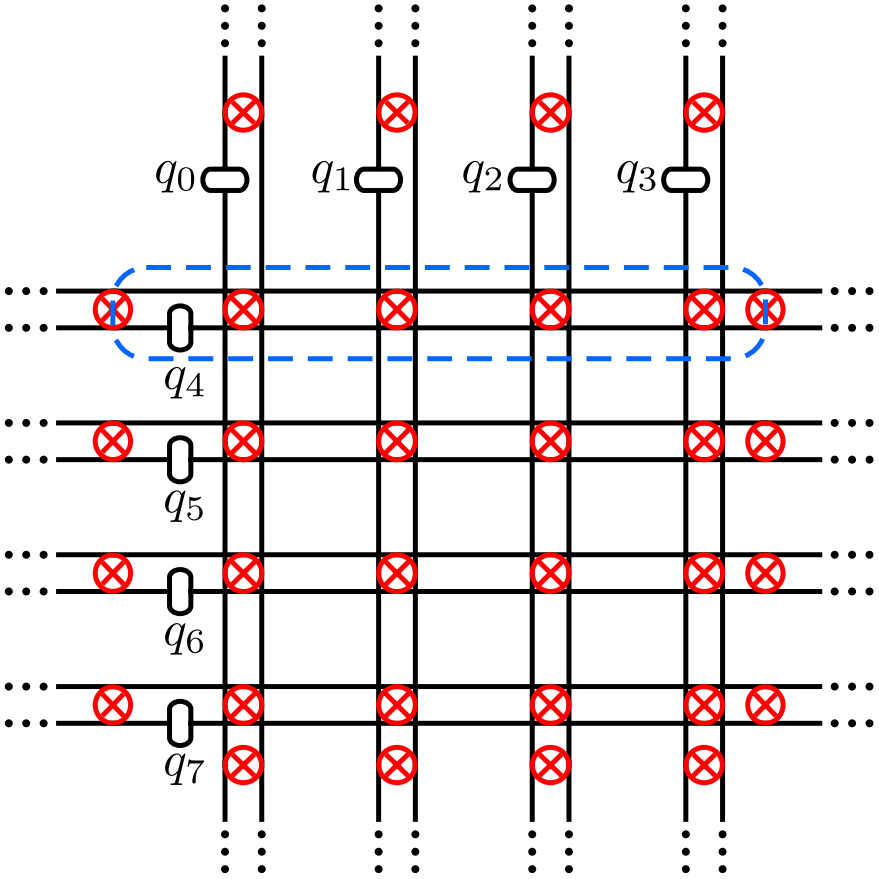


**Figure 2.3:** Sketch of the structure of one unit cell of the chip used in the D-Wave One. Each loop (circled by the blue box) stand for one qubit, denoted by $q_0, \ldots, q_7$. The qubits are pairwise coupled when they intersect (red circles). The dotted lines at the edge indicate the qubits of the unit cells next to one depicted here.

other one. For example $q_0$ and $q_4$ couple to each other. While $q_0$ also couples to the other horizontally aligned qubits, $q_5, q_6$ and $q_7$, $q_4$ couples to the vertically aligned ones, $q_1, q_2$ and $q_3$, thus there is no intersection between both sets.

## 2.3 Flux tunneling in the presence of noise

The potential of flux qubits has the form of a double-well potential, as shown in Fig. 2.2. In this potential, the states located in each well are separated by a large energy barrier of the order of the plasma frequency $\omega_p$, while the tunneling amplitude $\Delta$ is small, $\Delta \ll \omega_p$. In the regime of low energies, only the lowest states inside both wells can be occupied. Thus, the flux tunneling rate between the two wells experiences a resonant peak whenever the energy splitting $\epsilon$ between the lowest states inside each well becomes small, $\epsilon \ll \omega_p$. The dynamics of the system can then be described by the transition rates for tunneling between the lowest states, $|0\rangle$ and $|1\rangle$. To derive the transition rates we follow [10].

In the regime of low energies in the presence of noise the qubit can be described by the Hamiltonian

$$\mathcal{H} = \mathcal{H}_{\mathrm{S}} + \mathcal{H}_{\mathrm{B}} + \mathcal{H}_{\mathrm{int}} \,, \tag{2.30}$$

where $\mathcal{H}_{\mathrm{B}}$ is the bath Hamiltonian and

$$\mathcal{H}_{\mathrm{S}} = -\frac{1}{2}\left(\epsilon\sigma_z + \Delta\sigma_x\right) \tag{2.31a}$$

$$\mathcal{H}_{\mathrm{int}} = -\frac{1}{2}\sigma_z X \tag{2.31b}$$

are the qubit and interaction Hamiltonian respectively. In Eq. (2.31) $\epsilon$ and $\Delta$ are fixed parameters describing the energy splitting and the tunneling amplitude between the two states of the qubit and $X$ is an operator on the environment. When the environment is in thermal equilibrium at temperature $T$, the spectral density function of the noise operators is given by

$$\mathrm{S}(\omega) = \frac{1}{2\pi}\int_{-\infty}^{\infty} \mathrm{d}t\; \mathrm{e}^{\mathrm{i}\omega t}\,\langle X(t)X(0)\rangle \,, \tag{2.32}$$

where $\langle \ldots \rangle$ denotes the trace over all states of the environment.

In the incoherent regime $\Delta \ll W \ll \omega_p$, where $W$ is the noise-induced resonance width, the flux tunneling rate $\Gamma$ can be calculated by using the tunneling term $V = \Delta\sigma_x/2$, from Eq. (2.31a), as perturbation. Thus the lowest-order transition rates can be obtained using Fermi's Golden rule

$$\Gamma_{i\to f} = 2\pi\left|\langle i|V|f\rangle\right|^2 \delta\Big(E_i - E_f\Big) = \int_{-\infty}^{\infty} \mathrm{d}t\;\; \langle i(t)|V|f(t)\rangle\,\langle i(0)|V|f(0)\rangle \,, \tag{2.33}$$

where $|i\rangle$ and $|f\rangle$ denote the initial and final state of the total unperturbed system and, $E_i$ and $E_f$ the corresponding eigenenergy. The time evolution of these states, in the interaction picture, can be written as

$$|i(t)\rangle = U(t)\mathrm{e}^{\mathrm{i}\epsilon\sigma_z t/2}\,|i(0)\rangle \,, \tag{2.34}$$

where $U(t) = \mathcal{T}\exp[\mathrm{i}/2\;\sigma_z\int_{-\infty}^{t}\mathrm{d}\tau\; X(\tau)]$ with $\mathcal{T}$ denoting time ordering. After substituting Eq. (2.34) into Eq. (2.33) and summing over all initial and final states of the environment we get $\Gamma(\epsilon) \equiv \Gamma_{1\to0}(\epsilon) = \Gamma_{0\to1}(-\epsilon)$ with

$$\Gamma(\epsilon) = \frac{\Delta^2}{4}\int_{-\infty}^{\infty} \mathrm{d}t\; \mathrm{e}^{\mathrm{i}\epsilon t}\,\langle {U_-}^{\dagger}(t)U_+(t){U_+}^{\dagger}(0)U_-(0)\rangle \,, \tag{2.35}$$

where $U_\pm(t) = \mathcal{T}\exp[\pm\mathrm{i}/2\;\int_{-\infty}^{t}\mathrm{d}\tau\; X(\tau)]$. The correlator in Eq. (2.35) can be approximated, using Gaussian statistics, by expanding the operators $U_\pm(t)$ up to second order in $X$, averaging the result and exponentiating it back. Doing so we get

$$\langle {U_-}^{\dagger}(t)U_+(t){U_+}^{\dagger}(0)U_-(0)\rangle = \exp\left[\int_0^t \mathrm{d}\tau\;\int_{-\infty}^{0}\mathrm{d}\tau'\;\langle X(\tau)X(\tau')\rangle\right] . \tag{2.36}$$

In this expression the noise correlator can be expressed, using $X(t) = \mathrm{e}^{\mathrm{i}\mathcal{H}_\mathrm{B}t} X \mathrm{e}^{-\mathrm{i}\mathcal{H}_\mathrm{B}t}$, by the spectral density reducing Eq. (2.35) to

$$\Gamma(\epsilon) = \frac{\Delta^2}{4} \int\limits_{-\infty}^{\infty} \mathrm{d}t \, \mathrm{e}^{\mathrm{i}\epsilon t} \exp\left[ \int\limits_{-\infty}^{\infty} \mathrm{d}\omega \; \mathrm{S}(\omega) \frac{\mathrm{e}^{-\mathrm{i}\omega t} - 1}{\omega^2} \right] . \tag{2.37}$$

In the case, when the noise is strongly peaked at low-frequency the exponent $\mathrm{e}^{\mathrm{i}\omega t}$ can be expanded up to second order and Eq. (2.37) becomes

$$\Gamma(\epsilon) = \sqrt{\frac{\pi}{8}} \frac{\Delta^2}{W} \exp\left[ -\frac{(\epsilon - \epsilon_p)^2}{2W^2} \right] , \tag{2.38}$$

where

$$W^2 = \int \mathrm{d}\omega \; \mathrm{S}(\omega) \tag{2.39a}$$

$$\epsilon_p = \mathcal{P} \int \mathrm{d}\omega \; \frac{\mathrm{S}(\omega)}{\omega} . \tag{2.39b}$$

where $\mathcal{P}$ denotes principal value integration. Thus the noise with a significant low-frequency part leads to an Gaussian line-shape. Furthermore, we see that the noise not only broadens the resonance peak but also shifts it by a non-vanishing bias $\epsilon_p$ and thus splits the first resonance peak into two, for the two different directions of tunneling. Since the resonance width $W$ and the energy bias $\epsilon_p$ in Eq. (2.39) are, respectively, given by the symmetric and antisymmetric part of the noise, the two quantities are connected via the fluctuation-dissipation theorem. Thus for the strongly peaked low-frequency noise, where all relevant frequencies are small on the scale of the temperature $1/\beta$ and thus $\tanh(\beta\omega/2) \approx \beta\omega/2$, the energy bias is given by

$$\epsilon_p = \frac{1}{2} \beta W^2 . \tag{2.40}$$

The model derived above was extended in [11]. There, besides the strongly peaked low-frequency part $\mathrm{S}_{LF}(\omega)$ also a broadband high-frequency part $\mathrm{S}_{HF}$ of the spectral density was allowed, with $\mathrm{S}_{LF}(\omega) \gg \mathrm{S}_{HF}(\omega)$ for all relevant frequencies. Writing $\mathrm{S}(\omega) = \mathrm{S}_{LF}(\omega) + \mathrm{S}_{HF}(\omega)$ and expanding the exponential $\mathrm{e}^{\mathrm{i}\omega t}$ up to second order for the low-frequency part, Eq. (2.37) becomes

$$\Gamma(\epsilon) = \frac{\Delta^2}{4} \int\limits_{-\infty}^{\infty} \mathrm{d}t \, \mathrm{e}^{\mathrm{i}(\epsilon - \epsilon_p)t - W^2 t^2/2} \exp\left[ \int \mathrm{d}\omega \; \mathrm{S}_{HF}(\omega) \frac{\mathrm{e}^{\mathrm{i}\omega t} - 1}{\omega^2} \right] . \tag{2.41}$$

For the high-frequency part the noise spectral density can be expressed by the noise spectral function

$$\mathrm{S}_{HF}(\omega) = \frac{\mathrm{J}(\omega)}{1 - \mathrm{e}^{-\beta\omega}} . \tag{2.42}$$

Furthermore the spectral function can be expressed for an Ohmic environment by

$$\mathrm{J}(\omega) = \eta\omega \mathrm{e}^{-|\omega|/\omega_{HF}} , \tag{2.43}$$

where $\eta$ is a dimensionless parameter characterizing the strength of the noise and $\omega_{HF}$ is the cutoff of the high-frequency part. Substituting Eqs. (2.42) and (2.43) into Eq. (2.41) yields to

$$\Gamma(\epsilon) = \frac{\Delta_r}{4} \int_{-\infty}^{\infty} \mathrm{d}t \; \mathrm{e}^{\mathrm{i}(\epsilon-\epsilon_p)t - W^2t^2/2} \left[ \mathrm{i} \sinh \frac{t - \mathrm{i}/\omega_{HF}}{\beta} \right]^{-\eta} , \tag{2.44}$$

where $\Delta_r = (1/\beta\omega_{HF})^{\eta/2}\Delta$ is the renormalized tunneling amplitude. MRT measurements performed on a single flux qubit showed that the measured MRT rate coincides perfectly with Eq. (2.44) while Eq. (2.38) gives a good approximation for low energies [11].

## 2.4 Discussion about the D-Wave One

Although the skepticism about the functionality and reliability of the D-Wave One never died the discussion about it reached a new height, when the preprint of [12] was published in April 2013. In this article experiments on a D-Wave One with 108 superconducting flux qubits where performed. The benchmark was chosen to be the ability of finding the ground state of an Ising spin glass with Hamiltonian

$$H_{\mathrm{Ising}} = -\sum_{i<j} J_{ij}\sigma^i\sigma^j - \sum_i h_i\sigma^i \,, \tag{2.45}$$

where $\sigma^i = \pm 1$ are binary variables, $J_{ij}$ is the coupling between the $i$th and $j$th spin and $h_i$ a local field. Each Ising variable was mapped on the $\sigma_z$ of a qubit and thus the quantum mechanical Hamiltonian, with the transverse field needed for the adiabatic transition, reads

$$\mathcal{H} = -\,\mathrm{A}(t)\sum_i \sigma_x^i - \mathrm{B}(t)\left( \sum_{i<j} J_{ij}\sigma_z^i\sigma_z^j + \sum_i h_i\sigma_z^i \right) , \tag{2.46}$$

where $\mathrm{A}(t)$ and $\mathrm{B}(t)$ are the parameters of the annealing schedule. The parameters of the annealing schedule slowly change in time and were chosen in such a way that $\mathrm{A}(0) \gg \mathrm{B}(0)$ at the beginning and $\mathrm{A}(t_f) \ll \mathrm{B}(t_f)$ at the end of the annealing schedule.

In the experiment then 1000 different random instances, sets of $J_{ij} = \pm 1$, were selected and the local fields set to zero, $h_i = 0$. For each instance the annealing schedule was repeated 1000 times, counting the number of times in which the ground state was found. From that the success probability per instance was calculated. In Fig. 2.4 the histogram of the success probability of the D-Wave One obtained in the experiment is shown. There we can see that the success probability distribution has a bimodal structure with two peaks at zero and one. In addition to the experiment on the D-Wave One the experiment was also simulated using two different classical algorithms. The first algorithm is simulated annealing (SA), a Monte Carlo algorithm for classical annealing, and the second simulated quantum annealing (SQA), a quantum path integral Monte Carlo algorithm. Both simulations showed a different distribution of the success probability. While SA had a unimodal distribution, the distribution of SQA was bimodal with two peaks at zero and one, similar to the distribution of the D-Wave One. When the result from the D-Wave One was compared instance by instance with the one from SQA, it showed that both had a high correlation. In particular the same instances that had a low (high) success probability on the D-Wave One also had a low (high) success probability on SQA. From this correlation it was concluded that the D-Wave One must show quantum behavior.

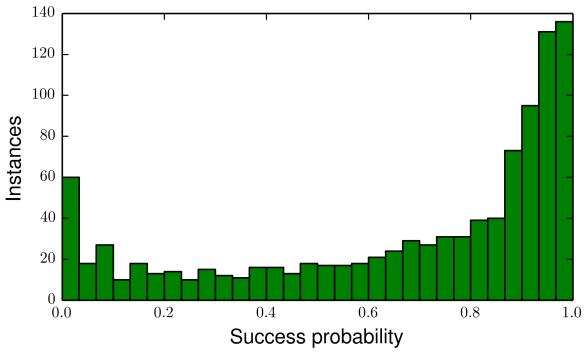


**Figure 2.4:** Histogram of the success probability of finding the ground state in 1000 different instances of an Ising spin glass with 108 spins of the D-Wave One. The success probability shows a bimodal distribution.

Shortly after the article discussed above was published, the group of Smolin et al. published the preprint of [13] in which they criticize the conclusion from the different success probability distribution to the quantum nature of the D-Wave One. In particular they stated that classical and quantum annealing cannot be compared with each other as both are of different nature. Simulated annealing proceeds by choosing a random initial state. Thus every run has different starting conditions and thus follows different trajectories. In contrast to classical annealing, quantum annealing always starts in the same ground state. From this follows that, in the ideal picture, the quantum annealer always follows the same trajectory and thus that there are only two possibilities, either it finds the ground state or it does not. This property can be directly seen in the bimodality of the success probability distribution. Thus they reason that the bimodality is more a sign for the reproducability than the quantumness of the D-Wave One.

To show that also classical models can lead to a bimodal success probability distribution, the group of Smolin et al. proposed the simple, classical SSSV-model, named after the authors of [14]. In this model the quantum mechanical spins from Eq. (2.46) are replaced by classical "compass needles" leading to the classical Hamilton function

$$H(t) = -\,\mathrm{A}(t)\sum_i \cos\theta_i - \mathrm{B}(t)\left(\sum_{i<j} J_{ij}\sin\theta_i\sin\theta_j + \sum_i h_i \sin\theta_i\right) . \tag{2.47}$$

With this model the experiment on the D-Wave One was simulated in [14] using the same instances as in the experiment.[1] The simulation also lead to a bimodal distribution like the D-Wave One and the SQA. Also the direct comparison of the simulation with the device showed correlations equivalent to the one between the device and SQA. From this Smolin et al. concluded that, although their model is most likely too simple to describe the D-Wave One completely, that classical models cannot be ruled out and thus that the results presented in [12] are no proof for the quantumness of the device.

Later, in September 2014, a group around Matthias Troyer and Daniel Lidar found in [16] that both models, SQA and SSSV, do not describe the D-Wave One. Therefore they developed new measures,

[1] The instances used in the experiment in [12] had been published in [15] as a response to the first article of the group of Smolin et al. .

besides the success probability distribution, on how to distinguish the results obtained from the device and the simulations, namely the spectrum of excited states and the found subset of the, in general degenerate, ground state. Both models, SQA and SSSV, cannot perfectly describe the observed properties found in the D-Wave One for these two measures. Furthermore they found that the SSSV-model and SQA correlate strongly with each other for these new measures, which can be explained as the SSSV-model can be derived as semi-classical limit of SQA. In their discussion they concluded that most likely the two models, SSSV and SQA, do not describe the D-Wave One. But they also stated that their analysis can have several potential loopholes. For example the Gaussian noise model used in the simulations could be too simplistic and thus that a better model for the noise could improve the correlation between the D-Wave One and SQA or the SSSV-model. Overall the question whether the D-Wave One experiences large-scale quantum effects remains open.

# Chapter 3
# Model

*In this chapter we derive our model for coupled qubits inside a quantum annealer with strong noise. Therefore, we derive and discuss its dynamics for a single qubit in Sec. 3.1. After that, we expand the model and discuss it for two coupled qubits in Sec. 3.2. Finally, we present the transition rates for the general case of N coupled qubits in Sec. 3.3 without further discussion.*

## 3.1 Single Qubit

Our model is based on the Hamiltonian Eq. (2.31). The difference is that the qubit no longer is in a fixed environment but inside a quantum annealer. This means that $\epsilon$ and $\Delta$ are no longer constant in time but rather given by $\mathrm{A}(t)$ and $\mathrm{B}(t)$, the parameters of the annealing schedule. With this Eq. (2.31a) reads

$$\mathcal{H}_\mathrm{S} = -\frac{1}{2}\left(\mathrm{A}(t)\,\sigma_x + h\,\mathrm{B}(t)\,\sigma_z\right) \tag{3.1}$$

where we additionally introduced $h$, a control knob to scale the energy. This small change makes a big difference as the annealing schedule is chosen such that at the beginning $\mathrm{A}(0) \gg \mathrm{B}(0)$ and at the end $\mathrm{A}(t_f) \ll \mathrm{B}(t_f)$. So at the beginning of the annealing schedule, if we ignore the noise, the A-term dominates the Hamiltonian Eq. (3.1) and thus its eigenstates are given in a $\sigma_x$-basis. When we now look at the end of the annealing schedule the B-term dominates and the eigenbasis is in the $\sigma_z$-basis. But that also means that in between the two terms swap their meaning. While at the end the B-term gives the energy and the A-term the tunneling amplitude, same as in [10], it is the other way round at the beginning.

In order to be able to keep track of the basis the system is in throughout the whole annealing time, we transform the system and describe it by the Pauli matrices $\hat{\tau}$. The Pauli matrices are chosen in such a way that the energy is always given by the $\tau_z$-term and the tunneling amplitude always by the $\tau_x$-term. At the beginning this transformation leads to the substitutions $\sigma_x \to \tau_z$ and $\sigma_z \to -\tau_x$, where the minus sign is needed to preserve the commutation relations. This describes nothing else but a rotation of the Pauli vector $\hat{\sigma}$ by an angle of $\theta = \pi/2$ in the $xz$-plane.

Up to this point we have only discussed the beginning and the end of the annealing schedule. Now let us extend the model to all times during the annealing schedule. Therefore we define a new time-dependent basis $\hat{\tau}$, rotated by an angle $\theta$ about the $y$-axiswith respect to the original basis $\hat{\sigma}$ i. e.

$$\hat{\tau} = R^{-1}\hat{\sigma} \tag{3.2}$$

where $R^{-1}$ is the inverse rotation matrix about the $y$-axis given by

$$R^{-1} = \begin{pmatrix} \cos\theta & 0 & -\sin\theta \\ 0 & 1 & 0 \\ \sin\theta & 0 & \cos\theta \end{pmatrix} . \tag{3.3}$$

The rotation angle $\theta$ is limited to $\theta \in [0, \pi/2]$ and in general is a function of time $\theta = \theta(t)$ given by the parameters of the annealing schedule. Applying the rotation in Eq. (3.2) results in the substitution

$$\begin{aligned} \sigma_x &\to \cos\theta\tau_x - \sin\theta\tau_z \\ \sigma_z &\to \sin\theta\tau_x + \cos\theta\tau_z \,. \end{aligned} \tag{3.4}$$

Although the exact time dependency of $\theta$ is still unknown, we can see that we can reproduce the behaviour above when we set the boundary conditions $\theta(0) = \pi/2$ and $\theta(t_f) = 0$. Nevertheless we must not forget that up until now we have considered our system to be disconnected from the environment. Hence the picture might change if we allow the environment to couple to the qubit.

Let us now study our model in more detail. Therefore we make the ansatz

$$\mathcal{H} = \mathcal{H}_\mathrm{S} + \mathcal{H}_\mathrm{B} + \mathcal{H}_\mathrm{int} \,, \tag{3.5}$$

where $\mathcal{H}_\mathrm{S}$ is the system Hamiltonian Eq. (3.1), $\mathcal{H}_\mathrm{B}$ is the bath Hamiltonian and $\mathcal{H}_\mathrm{int}$ is the interaction Hamiltonian of the system with the bath Eq. (2.31b), and insert the substitution Eq. (3.4). After sorting the terms for the new Pauli matrices the system and interaction Hamiltonian changes to

$$\mathcal{H}_\mathrm{S} = -\frac{1}{2}\left(\Delta\tau_x + \epsilon\tau_z\right) \tag{3.6a}$$

$$\mathcal{H}_\mathrm{int} = -\frac{1}{2}\left(\sin\theta\tau_x + \cos\theta\tau_z\right) X \tag{3.6b}$$

where

$$\epsilon(\theta) = -\,\mathrm{A}\sin\theta + h\,\mathrm{B}\cos\theta \tag{3.7a}$$

$$\Delta(\theta) = \mathrm{A}\cos\theta + h\,\mathrm{B}\sin\theta \,. \tag{3.7b}$$

In Eq. (3.6b) we can see another interesting new property of our system compared to [10], as our system now contains not only a longitudinal but also a transverse coupling to the bath.

Our ansatz still depends on the unknown bath Hamiltonian. To get rid of it we transform to the interaction picture. Therefore we assume the bath to be in thermal equilibrium at temperature $T$ and thus its Hamiltonian is independent of time. With this the unitary transformation can be written as

$$U(t) = \mathrm{e}^{\mathrm{i}\mathcal{H}_\mathrm{B} t} \tag{3.8}$$

and the Hamiltonian becomes

$$\begin{aligned} \mathcal{H}_I &= U\mathcal{H}U^\dagger + i\dot{U}U^\dagger \\ &= -\frac{\Delta}{2}\tau_x - \frac{\epsilon}{2}\tau_z - \frac{1}{2}(\sin\theta\tau_x + \cos\theta\tau_z)X_I(t) \end{aligned} \tag{3.9}$$

where $X_I(t) = U(t)XU^\dagger(t)$ is a bath operator in the interaction picture. In order to keep the notation clean let us drop the index $I$ for the interaction picture again.

To describe the dynamics of the system let us first ignore the transverse coupling in Eq. (3.9) and have a look at the noise term. By ignoring the transverse coupling the noise has its major contribution in the original basis, i. e. when $\theta = 0$. In this basis the energy is given by $\epsilon = \mathrm{B}$ and the tunneling amplitude by $\Delta = \mathrm{A}$. Thus the strength of the noise term is determined by $\mathrm{S}(\omega = \mathrm{B})$, where $\mathrm{S}(\omega)$ is the noise spectral density. Hence when we look at the beginning of the annealing schedule the noise strength is given by $\mathrm{S}(0)$. In [11] it was shown that the noise on a qubit is strongly peaked at $\omega = 0$ and thus it is save to say that $\Delta \ll \mathrm{S}(0) \ll \omega_p$ at the beginning. When time progresses the energy rises and thus $\mathrm{S}(\epsilon)$ becomes smaller. But at the same time also the tunneling term becomes smaller. Thus we assumed that $\Delta \ll \epsilon + \mathrm{S}(\epsilon) \ll \omega_p$ throughout the annealing schedule. From this follows that the $\tau_z$-terms dominate and thus that the tunneling term can be taken to be a small perturbation. Furthermore, as $\epsilon + \mathrm{S}(\epsilon) \ll \omega_p$, the occupation of excited states in the wells are strongly suppressed and the dynamics of the system can be reduced to the two lowest states even in the presence of noise. Therefore the flux tunneling rates $\Gamma$ can then be calculated in lowest-order perturbation theory in the tunneling term $V = \Delta\tau_x/2$ analog to [10].

Starting from Fermi's Golden rule

$$\Gamma_{i\to f} = 2\pi \left|\langle i|V|f\rangle\right|^2 \delta\Big(E_i - E_f\Big) = \int_{-\infty}^{\infty} \mathrm{d}t \ \langle i(t)|V|f(t)\rangle \langle f(0)|V|i(0)\rangle \tag{3.10}$$

where $|i\rangle$ ($|f\rangle$) denote the initial (final) state of the total unperturbed system, e. g. $|i\rangle = |i_B\rangle\,|1\rangle$, with eigenenergy $E_i$ ($E_f$). The time evolution of these unperturbed states is given by

$$|i(t)\rangle = \mathcal{T} \exp\left[\frac{\mathrm{i}}{2}\int_{-\infty}^{t} \mathrm{d}t' \ \Big(\cos\theta X(t')\tau_z + \epsilon\tau_z\Big)\right] |i(0)\rangle = U(t)\mathrm{e}^{\mathrm{i}\epsilon\tau_z t/2}\,|i(0)\rangle \ . \tag{3.11}$$

Here $U(t) = \mathcal{T}\exp[\mathrm{i}/2\,\tau_z \cos\theta \int_{-\infty}^{t} \mathrm{d}t' \ X(t')]$ is the time evolution operator where $\mathcal{T}$ denotes time ordering. At this point we took the rotation angle $\theta$, and with that also the energy $\epsilon(\theta)$, to be constant in time. This assumption is justified as $\epsilon$ and $\theta$ only change on the time scale given by the annealing schedule which is much slower than the relaxation processes of the system, which are of interest here. The transition rates are then given by the sum over all possible initial (with equilibrium density matrix $\rho$) and final states of the bath. Inserting Eq. (3.11) in Eq. (3.10), using $\tau_z\,|0\rangle = |0\rangle\,, \tau_z\,|1\rangle = -\,|1\rangle$, and summing over the bath states leads to

$$\begin{aligned}\Gamma_{1\to 0}(\epsilon) &= \sum_{i_B, f_b} \rho \int_{-\infty}^{\infty} \mathrm{d}t \ \langle i(t)|V|f(t)\rangle \langle f(0)|V|i(0)\rangle \\ &= \frac{\Delta^2}{4}\int_{-\infty}^{\infty} \mathrm{d}t\, \mathrm{e}^{\mathrm{i}\epsilon t} \langle U_-^\dagger(t) U_+(t) U_+^\dagger(0) U_-(0)\rangle\end{aligned} \tag{3.12}$$

where $\langle\cdots\rangle = \mathrm{Tr}_B\{\rho\cdots\}$ is the partial trace over the bath states and $U_\pm(t) = \mathcal{T}\exp[\pm i/2\cos\theta\int_{-\infty}^{t}\mathrm{d}t' \ X(t')]$. The correlator in Eq. (3.12) can be calculated in the Gaussian approximation by expanding the time evolution operator $U_\pm(t)$ up to the second order in $X$, averaging the result and exponentiating it back. This gives

$$\langle U_\mp^\dagger(t) U_\pm(t) U_\pm^\dagger(0) U_\mp(0)\rangle = \exp\left[\cos^2\theta \int_0^t \mathrm{d}t' \int_{-\infty}^{0} \mathrm{d}t'' \ \langle X(t')X(t'')\rangle\right] . \tag{3.13}$$

In this approximation the sign in $U_{\pm}(t)$ does not make a difference. Thus we can define the flip rate $\Gamma_{\mathrm{F}}(\epsilon) \equiv \Gamma_{1\to0}(\epsilon) = \Gamma_{0\to1}(-\epsilon)$. Remembering that in the interaction picture $X(t) = \mathrm{e}^{\mathrm{i}\mathcal{H}_{\mathrm{B}}t} X \mathrm{e}^{-\mathrm{i}\mathcal{H}_{\mathrm{B}}t}$ the integrals on the RHS in Eq. (3.13) can be rewritten to

$$\int_0^t \mathrm{d}t' \int_{-\infty}^0 \mathrm{d}t''\ \langle X(t')X(t'')\rangle = \sum_{n_B,m_B} \rho_n \int_0^t \mathrm{d}t' \int_{-\infty}^0 \mathrm{d}t''\ \langle n_B|X(t')|m_B\rangle \langle m_B|X(t'')|n_B\rangle \tag{3.14}$$

$$= \sum_{n_B,m_B} \rho_n \left|\langle n_B|X|m_B\rangle\right|^2 \int_0^t \mathrm{d}t' \int_{-\infty}^0 \mathrm{d}t''\, \mathrm{e}^{-\mathrm{i}(\mathcal{E}_m-\mathcal{E}_n)t'} \mathrm{e}^{\mathrm{i}(\mathcal{E}_m-\mathcal{E}_n)t''} \tag{3.15}$$

$$= \int_{-\infty}^{\infty} \mathrm{d}\omega \sum_{n_B,m_B} \rho_n \left|\langle n_B|X|m_B\rangle\right|^2 \delta\big(\omega - (\mathcal{E}_m - \mathcal{E}_m)\big) \frac{\mathrm{e}^{-\mathrm{i}\omega t}-1}{\omega^2} \tag{3.16}$$

$$= \int_{-\infty}^{\infty} \frac{\mathrm{d}\omega}{2\pi}\, \mathrm{S}(\omega) \frac{\mathrm{e}^{-\mathrm{i}\omega t}-1}{\omega^2} \tag{3.17}$$

where $\mathcal{E}_n$ is an eigenenergy of the Bath eigenstate $|n_B\rangle$, $\rho_n$ the equilibrium probability density and $\mathrm{S}(\omega)$ the noise spectral density. Inserting Eq. (3.17) into Eq. (3.12) the rates finally become

$$\Gamma_{\mathrm{F}}(\epsilon) = \frac{\Delta^2}{4} \int_{-\infty}^{\infty} \mathrm{d}t\, \mathrm{e}^{-\mathrm{i}\epsilon t} \exp\left[\cos^2\theta \int_{-\infty}^{\infty} \frac{\mathrm{d}\omega}{2\pi}\, \mathrm{S}(\omega) \frac{\mathrm{e}^{-\mathrm{i}\omega t}-1}{\omega^2}\right] \tag{3.18}$$

which, without the cosine, is one result from [10].

The result from Eq. (3.17) can even further be rewritten. Therefore let us express the noise spectral density by

$$\mathrm{S}(\omega) = \frac{\mathrm{J}(\omega)}{1-\mathrm{e}^{-\beta\omega}} \tag{3.19}$$

with the noise spectral function $\mathrm{J}(\omega)$ and the inverse temperature $\beta$. Inserting Eq. (3.19) into Eq. (3.17) and splitting the integral for negative and positive frequencies leads to

$$\int_{-\infty}^{\infty} \frac{\mathrm{d}\omega}{2\pi}\, \mathrm{S}(\omega) \frac{\mathrm{e}^{-\mathrm{i}\omega t}-1}{\omega^2} = -\int_0^{\infty} \frac{\mathrm{d}\omega}{2\pi} \frac{\mathrm{J}(\omega)}{\omega^2} \left(\frac{1-\mathrm{e}^{-\mathrm{i}\omega t}}{1-\mathrm{e}^{-\beta\omega}} - \frac{1-\mathrm{e}^{\mathrm{i}\omega t}}{1-\mathrm{e}^{i\beta\omega}}\right). \tag{3.20}$$

After reducing the fractions to a common denominator, expressing the complex exponent by sine and cosine, and sorting some terms the final result becomes

$$-\mathrm{J}(t) \equiv -\int_{-\infty}^{\infty} \frac{\mathrm{d}\omega}{2\pi}\, \mathrm{S}(\omega) \frac{\mathrm{e}^{-\mathrm{i}\omega t}-1}{\omega^2} = \int_0^{\infty} \frac{\mathrm{d}\omega}{2\pi} \frac{\mathrm{J}(\omega)}{\omega^2} \left((1-\cos\omega t)\coth\frac{\beta\omega}{2} + \mathrm{i}\sin\omega t\right) \tag{3.21}$$

the typical result from $P(E)$-Theory [17]. And thus the final transition rate reads

$$\Gamma_{\mathrm{F}}(\epsilon) = \frac{\Delta^2}{4} \int_{-\infty}^{\infty} \mathrm{d}t\, \mathrm{e}^{-\cos^2\theta\, \mathrm{J}(t)} \mathrm{e}^{-\mathrm{i}\epsilon t}. \tag{3.22}$$

Up until now we have neglected the transverse coupling in Eq. (3.9). So let us now discuss what effects it causes. Therefor let us again have a look at the strength of the noise first. The transverse coupling has its main contribution in the fully rotated basis, i. e. when $\theta = \pi/2$. In this basis the energy is given by $\epsilon = \mathrm{A}$ and the tunneling amplitude by $\Delta = \mathrm{B}$. So now the noise strength is given by $\mathrm{S}(\omega = \mathrm{A})$. But that means, in combination with the noise being strongly peaked at low frequencies, that at the beginning $\mathrm{S}(\epsilon) \ll \epsilon$. Thus the transverse coupling term can now be taken as perturbation.[1] So we can again use Fermi's Golden rule Eq. (3.10) but this time the perturbation is given by the coupling term in the interaction Hamiltonian i. e. $V = \sin\theta\tau_x X(t)/2$. With this we get

$$\Gamma_{\mathrm{D}}(\epsilon) \equiv \Gamma_{1\to 0}(\epsilon) = \sum_{i_B, f_b} \rho \int_{-\infty}^{\infty} \mathrm{d}t \ \langle i(t)|V|f(t)\rangle \langle f(0)|V|i(0)\rangle \tag{3.23}$$

$$= \frac{\sin^2\theta}{4} \int_{-\infty}^{\infty} \mathrm{d}t \ \sum_{i_B, f_B} \rho \langle i_B|X(t)X(0)|i_B\rangle \, \mathrm{e}^{\mathrm{i}\epsilon t} \tag{3.24}$$

$$= \frac{\sin^2\theta}{4} \mathrm{S}(\epsilon) \tag{3.25}$$

$$= \frac{\sin^2\theta}{4} \frac{\mathrm{J}(\epsilon)}{1 - \mathrm{e}^{-\beta\epsilon}} \,. \tag{3.26}$$

where we inserted Eq. (3.19) in Eq. (3.25) at the last step. Analog to Eq. (3.26) the decay rate for the transition $0 \to 1$ can be calculated to

$$\Gamma_{0\to 1}(\epsilon) = \Gamma_{\mathrm{D}}(-\epsilon) = \mathrm{e}^{-\beta\epsilon}\Gamma_{\mathrm{D}}(\epsilon) \tag{3.27}$$

where we have used the Fluctuation-Dissipation Theorem in the last step.

Further we know from basic decoherence theory that the off-diagonal elements of the density matrix of a two level system for pure transverse coupling are given by

$$\rho_{10}(t) = \rho_{10}(0) \exp\left[ -\frac{\Gamma_{\mathrm{D}}(\epsilon) + \Gamma_{\mathrm{D}}(-\epsilon)}{2} \ |t| \right] \mathrm{e}^{-\mathrm{i}\epsilon t} \,. \tag{3.28}$$

But when we Fourier transform this into energy space we see that this simply resolves into a renormalization of the energy

$$\epsilon \to \epsilon + \mathrm{i}\frac{\Gamma_{\mathrm{D}}(\epsilon) + \Gamma_{\mathrm{D}}(-\epsilon)}{2} \,. \tag{3.29}$$

Thus we define the line broadening $\Gamma_{\mathrm{W}}$ as

$$\Gamma_{\mathrm{W}}(\epsilon) = \frac{1}{2}\left(\Gamma_{\mathrm{D}}(\epsilon) + \Gamma_{\mathrm{D}}(-\epsilon)\right) \tag{3.30}$$

$$= \frac{1}{2}\left(1 + \mathrm{e}^{\mathrm{i}\beta\epsilon}\right)\Gamma_{\mathrm{D}}(\epsilon) \tag{3.31}$$

$$= \frac{\sin^2\theta}{8} \mathrm{J}(\epsilon) \coth\frac{\beta\epsilon}{2} \tag{3.32}$$

[1] The argument breaks down for later times. But as we assume that the system is only at the beginning of the annealing schedule in the fully rotated basis the error made by this assumption should be small.

and renormalize the energy in Eq. (3.22) analog to Eq. (3.29). So the flip rate now reads

$$\Gamma_{\mathrm{F}}(\epsilon) = \frac{\Delta^2}{4} \int_{-\infty}^{\infty} \mathrm{d}t \, \mathrm{e}^{-\cos^2\theta \, \mathrm{J}(t)} \mathrm{e}^{-\mathrm{i}\epsilon t} \mathrm{e}^{-\Gamma_{\mathrm{W}}(\epsilon)|t|} \,. \tag{3.33}$$

With the discussion above the total rate for single flip events is given by the sum of the decay and flip rate i. e.

$$\Gamma_{\mathrm{SF}}(\epsilon) = \Gamma_{\mathrm{D}}(\epsilon) + \Gamma_{\mathrm{F}}(\epsilon) \,. \tag{3.34}$$

Both parts of Eq. (3.34) depend on the noise spectral function $\mathrm{J}(\omega)$, which still has to be modeled. In [11] measurements on a single flux qubit have been performed. There it was shown that the noise consists of two Ohmic parts, where one of the parts is strongly peaked at low frequencies (LF) and the other is broadband at high frequencies (HF). So we use an ansatz with the sum of two Ohmic spectral functions with a Lorentzian cutoff

$$\mathrm{J}(\omega) = \omega \left( \eta_{LF} \frac{\omega_{LF}}{\omega_{LF}^2 + \omega^2} + \eta_{HF} \frac{\omega_{HF}}{\omega_{HF}^2 + \omega^2} \right) \tag{3.35}$$

where $\eta_i$ is the dimensionless coupling strength and $\omega_i$ the cutoff frequency.

Now let us numerically evaluate the rates. Therefore we need to determine some plot parameters. For the calculation we normalize them to the maximal energy given by the annealing schedule i. e. such that $5\,\mathrm{GHz} = 1$ [12]. With this $\eta_{HF} = 0.41 \approx 0.5$ and $k_B T = 21\,\mathrm{mK}\, k_B \approx 0.5\,\mathrm{GHz} = 0.1$ can be taken from [11]. Furthermore we assumed that the low frequency noise couples much stronger to the qubit than the high frequency noise and thus $\eta_{LF} = 5$ and $\eta_{HF} = 0.5$ were chosen. For the cutoff frequency we took $\omega_{LF} = 0.1$ and $\omega_{HF} = 10$.

In Fig. 3.1 the flip rate $\Gamma_{\mathrm{F}}$, Eq. (3.33), is plotted as a function of energy $\epsilon$ and rotation angle $\theta$. It is nice to see, that the rate at the beginning has a broad peak for positive energies at small angles and slowly moves back to energies around zero and large angles. The double peak structure at $\epsilon \approx 0$ is due to the line broadening $\Gamma_{\mathrm{W}}$. It has its maximal contribution when $\theta = \pi/2$ and only depends on the annealing schedule via the tunneling amplitude $\Delta$. Because of $\Delta(\theta = \pi/2) = \mathrm{B}$ its impact in the beginning is minimal and slowly grows with the simulation time. Finally one can see in the plots that at the end of the schedule the flip rate becomes exactly zero at $\theta = 0$ independent of the energy $\epsilon$. This is important as at the end of the annealing schedule the state of the qubits has to be in the original basis, i. e. $\theta(t_f) = 0$, and the state has to be frozen in a given state, i. e. the transition rate is zero.

The decay rate $\Gamma_{\mathrm{D}}$, Eq. (3.26), is shown in Fig. 3.2. In contrast to the flip rate the decay rate does not directly depend on the annealing schedule. This resembles our assumption from above, that the effects causing the noise take place on a time scale much faster than the annealing schedule. Thus the qubit sees a static noise background and has a constant decay rate on the time scale given by the annealing schedule. The plot shows that the decay rate has, as expected, a peak at $\epsilon \approx 0$ and drops off exponentially for negative while reaching a plateau for positive energies. As the decay rate only depends on the rotation angle $\theta$ via its prefactor its dependency is easy to understand. Due to the prefactor the decay rate, just as the flip rate at $t/t_f = 1$, vanishes for $\theta = 0$. This arises directly from our model as the origin of the decay rate is the transverse coupling in the the interaction Hamiltonian Eq. (3.6b) which only appears after leaving the original basis i. e. when $\theta \neq 0$.

Finally the total rate for single flip events Eq. (3.34) is shown in Fig. 3.3 and does not come with a further surprise. The only interesting fact to see is that both, the flip and decay rate, are of the same

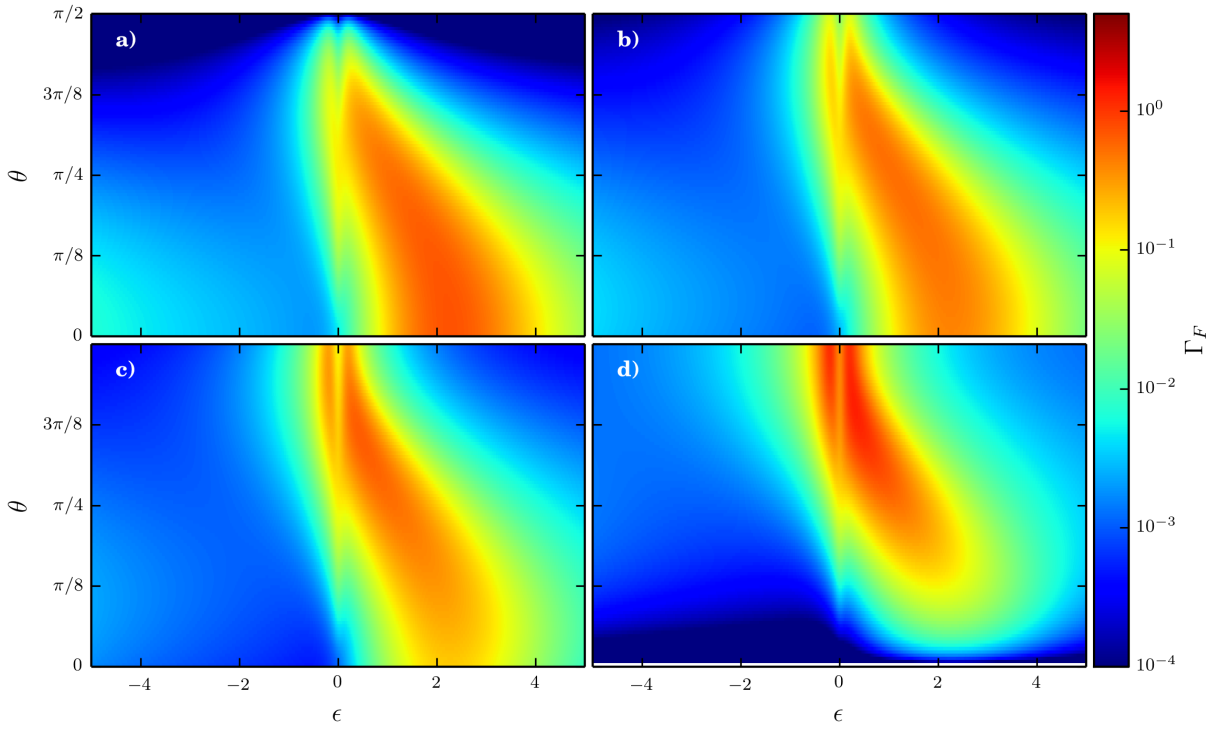


**Figure 3.1:** Plot of the flip rate Eq. (3.33) as a function of $\epsilon$ and $\theta$ for a) $t/t_f = 0$, b) $t/t_f = 0.25$, c) $t/t_f = 0.5$ and d) $t/t_f = 1$ with parameters $\beta = 10, \eta_{LF} = 5, \omega_{LF} = 0.1, \eta_{HF} = 0.5$, $\omega_{HF} = 10$ and, $h = 1$ and assuming a linear annealing schedule i. e. $\mathrm{A} = 1 - t/t_f$ and $\mathrm{B} = t/t_f$.

order of magnitude and thereby both have to be considered when we want to determine the optimal rotation angle.

To do so lets recall that in general the rotation angle $\theta$ is expected to be a function of time depending on the annealing schedule i. e. the parameters $\mathrm{A}(t)$ and $\mathrm{B}(t)$. Furthermore transition rates, in lowest order, have the general form

$$\Gamma = g^2 \int_{-\infty}^{\infty} \mathrm{d}t \, \mathrm{e}^{\gamma|t|} \mathrm{e}^{\mathrm{i}\Delta E t} \propto \frac{g^2}{\gamma} \tag{3.36}$$

where $g$ is the matrix element connecting the states and $\gamma$ is the lifetime of the state [18]. While the preferred basis is given where $g/\gamma$ has its minimum. Unfortunately both quantities are hard to come by, especially when one considers systems with more than one qubit. In order to get an impression on how the angle behaves we decided to take the angle $\theta^{\min}$, where the total transition rate $\Gamma_{\mathrm{tot}}$ out of a given state has its minimum as the preferred angle. For the single qubit case the total rate is simply given by the single flip rate i. e. $\Gamma_{\mathrm{tot}} = \Gamma_{\mathrm{SF}}$. In Fig. 3.4 the angle $\theta^{\min}$ is plotted versus the normalized time $t/t_f$, with annealing time $t_f$, assuming a linear annealing schedule i. e. $\mathrm{B}(t) = t/t_f, \mathrm{A}(t) = 1 - \mathrm{B}(t)$. The plots show that the two cases when the qubit is in state $|1\rangle$, where it lowers its energy by the transition, and when it is in $|0\rangle$, where it raises its energy by the transition, have a different behaviour. If it is in $|0\rangle$ the qubit prefers the $\sigma_z$-basis during the whole annealing schedule while if it is in state $|1\rangle$ it starts out in the $\sigma_x$-basis and then jumps at $t/t_f \approx 0.3$ to the $\sigma_z$-basis.

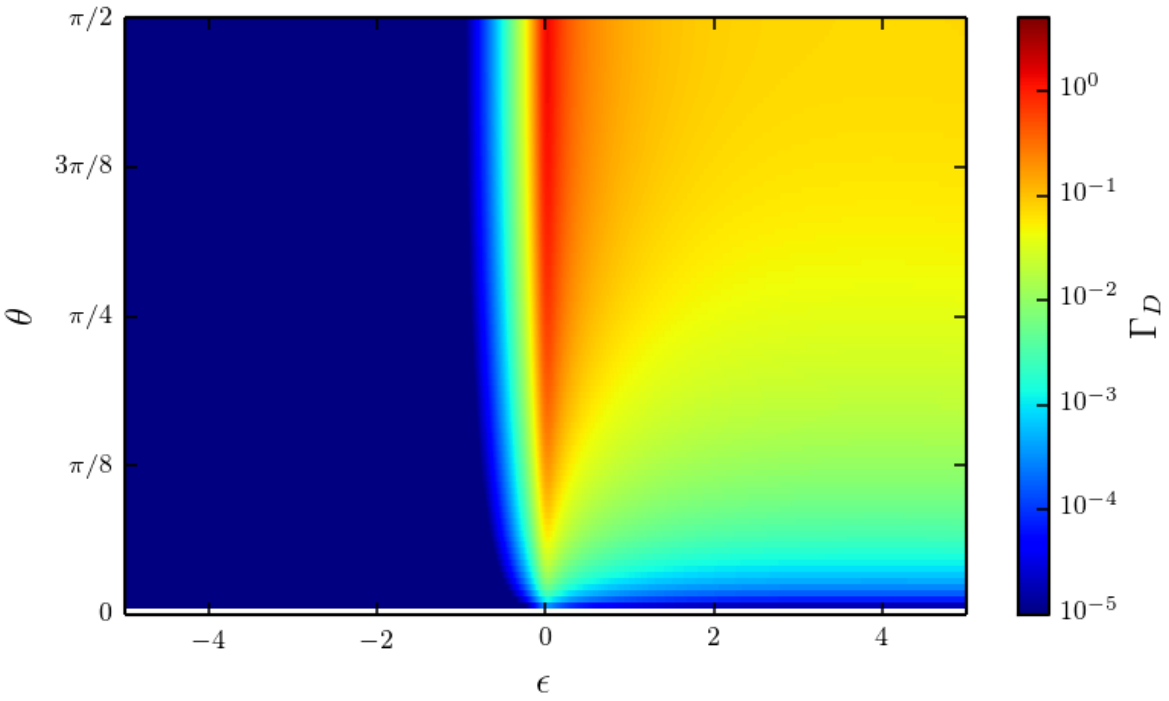


**Figure 3.2:** Plot of the decay rate Eq. (3.26) as a function of $\epsilon$ and $\theta$ with parameters $\beta = 10, \eta_{LF} = 5, \omega_{LF} = 0.1, \eta_{HF} = 0.5$, $\omega_{HF} = 10$ and $h = 1$.

The reason for this behaviour can already be presumed in Fig. 3.3 when one remembers that $\epsilon$ is not an independent variable but rather depends on $\theta$ as given in Eq. (3.7a).

Let us first concentrate on the case, when the qubit is in state $|0\rangle$ with energy $-\epsilon$. Then the energy $-\epsilon$ starts purely positive and the rate is dominated by the plateau of the decay rate. Thus in order to minimize the total rate, the decay rate has to be minimized, which is equivalent to go to $\theta = 0$. At this point the flip rate has a finite but small value. When time progresses several things happen. First at $\theta = \pi/2$, where $\Delta = \mathrm{B}$, the flip rate increases while the energy $-\epsilon$ moves to 0 and thus approaching the peak of the decay rate. At the same time at $\theta = 0$, where $\Delta = \mathrm{A}$, the flip rate slowly decreases and $-\epsilon$ moves to $-1$ and thus even further away from the vanishing peak. Adding those effect up leads to the fact that the single flip rate has its minimum at $\theta = 0$ throughout the annealing time.

On the other hand, when the qubit is in state $|1\rangle$ the corresponding energy $\epsilon$ starts purely negative and thus in the region of the exponential decrease in the decay rate. Thus the flip rate dominates when minimizing the total rate. But in contrast to the decay rate the flip rate has its minimum at the beginning at $\theta = \pi/2$. When time progresses exactly the same effects as in the $|0\rangle$ case take place. But in our case this now means that the rate in the rotated basis at $\theta = \pi/2$, in which we are in, slowly increases while the rate in the original basis slowly decreases. At some point both have the same value and the state flips from the rotated to the original basis i. e. from $\theta = \pi/2$ to $\theta = 0$.

This behaviour can be seen in more detail in Fig. 3.5. There one can also see, that the actual value of the tunneling amplitude $\Delta$ does not play a role in the discussion. More important is the sign of the energy $\epsilon$, which determines whether the rate has to be minimized via the decay or the flip rate.

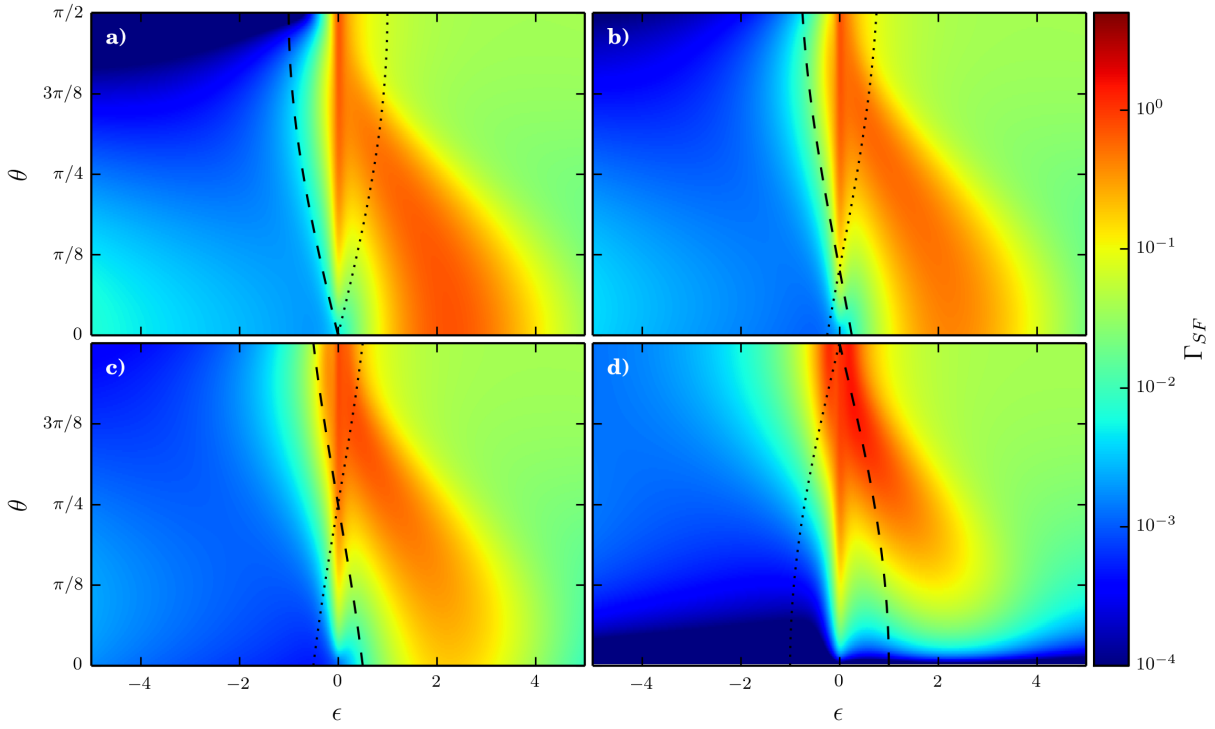


**Figure 3.3:** Plot of the single flip rate Eq. (3.34) as a function of $\epsilon$ and $\theta$ for a) $t/t_f = 0$, b) $t/t_f = 0.25$, c) $t/t_f = 0.5$ and d) $t/t_f = 1$ with parameters $\beta = 10, \eta_{LF} = 5, \omega_{LF} = 0.1, \eta_{HF} = 0.5, \omega_{HF} = 10$ and, $h = 1$ and assuming a linear annealing schedule i. e. $\mathrm{A} = 1 - t/t_f$ and $\mathrm{B} = t/t_f$. The black dashed (dotted) line is the energy $\epsilon$ $(-\epsilon)$ defined in Eq. (3.7a) for the case when the qubit is in state $|1\rangle$ $(|0\rangle)$ at the given time.

## 3.2 Two Qubits

Now let us extend our model for a case with two qubits. To describe the qubits we again use the ansatz Eq. (3.1) and couple the qubits with a coupling constant $J_{12}$ which we allow to be $J_{12} = \pm 1$. Thus our Hamiltonian in the interaction picture reads

$$\mathcal{H} = -\frac{\mathrm{A}(t)}{2}(\sigma_x^1 + \sigma_x^2) - \frac{\mathrm{B}(t)}{2}(h_1\sigma_z^1 + h_2\sigma_z^2 + J_{12}\sigma_z^1\sigma_z^2) - \frac{1}{2}\sigma_z^1 X_1(t) - \frac{1}{2}\sigma_z^2 X_2(t) \tag{3.37}$$

where $\sigma_{x,z}^i$ denotes Pauli matrices and $X_i$ the noise operator acting on the $i$-th qubit. As for the single qubit case we we change to the new basis depending on the annealing schedule. Because both qubits could prefer a different basis set during the process we introduce an angle $\theta_i$ which denotes the rotation angle of the $i$th qubit. After applying the basis transformation the Hamiltonian can be written in the following form

$$\mathcal{H} = \mathcal{H}_1 + \mathcal{H}_2 + \mathcal{H}_{12}\,. \tag{3.38}$$

Here $\mathcal{H}_i$ is of the form of the single qubit Hamiltonian Eq. (3.9) with the difference that $\mathcal{H}_i$ also has a contribution from the coupling. This contribution can be added to the energy and tunneling amplitude

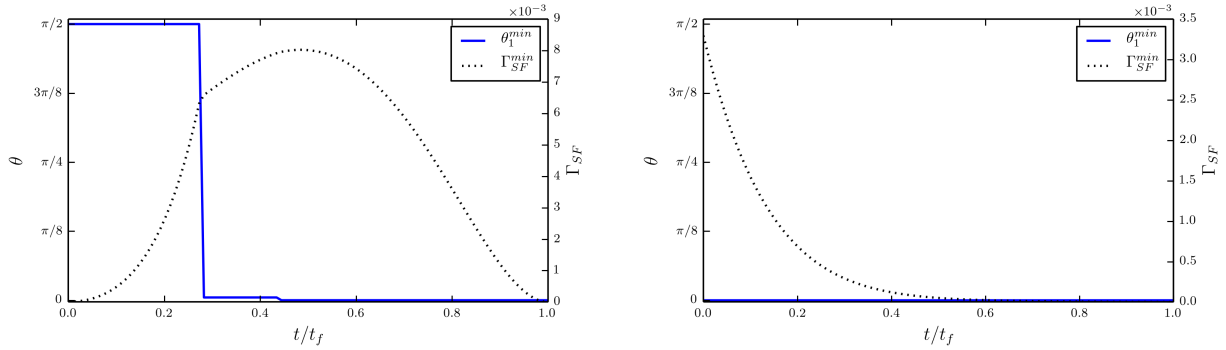


**(a)** **(b)**

**Figure 3.4:** Plots of the minimal rate $\Gamma_{\mathrm{SF}}^{\mathrm{min}}$ and the corresponding angle $\theta^{\mathrm{min}}$ when the system is in state (a) $|1\rangle$ and, (b) $|0\rangle$. The data was calculated using Eq. (3.34) with a linear annealing schedule, i. e. $\mathrm{B} = t/t_f$ and $\mathrm{A} = 1 - \mathrm{B}$, and the parameters $\beta = 10, \eta_{LF} = 5, \omega_{LF} = 0.1, \eta_{HF} = 0.5$, $\omega_{HF} = 10$ and, $h = 1$.

respectively and thus

$$\epsilon(\theta) \to \epsilon(\theta_i) + \frac{\mathrm{B}}{2} J_{ij} \cos\theta_i \cos\theta_j \tau_z^j \equiv \epsilon_i + \tilde{\epsilon}_i J_{ij} \tau_z^j \tag{3.39a}$$

$$\Delta(\theta) \to \Delta(\theta_i) + \frac{\mathrm{B}}{2} J_{ij} \sin\theta_i \cos\theta_j \tau_z^j \equiv \Delta_i + \tilde{\Delta}_i J_{ij} \tau_z^j \,, \tag{3.39b}$$

where $i, j = 1, 2$, $i \neq j$ and $\epsilon_i$ and $\Delta_i$ as defined in Eq. (3.7), has to be substituted. In addition to the diagonal part we find $\mathcal{H}_{12}$ which comes from the mixing term of the transformation in the interaction and reads

$$\mathcal{H}_{12} = -\frac{\mathrm{B}}{2} J_{12} \sin\theta_1 \sin\theta_2 \tau_x^1 \tau_x^2 \equiv -\frac{M_{12}}{2} \tau_x^1 \tau_x^2 \,. \tag{3.40}$$

It describes the situation when both qubits flip at the same time.

Now let us take a look at the dynamics of the system. For single flip events the overall structure of the Hamiltonian did not change. Therefore we can directly take the results from Sec. 3.1 and only have to consider the substitution in Eq. (3.39). From this follows that the energy as well as the tunneling amplitude now depend on the state of the second qubit and the coupling constant. Hence the transition rates can now have two different values, as $J_{ij}\tilde{\tau}_z^j = \pm 1$ where $\tilde{\tau}_z^j$ is the eigenvalue of the $j$-th spin. Considering this the transition rates for single flip events now read

$$\Gamma_{\mathrm{F},\pm}^i = \frac{(\Delta_i \pm \tilde{\Delta}_i)^2}{4} \int_{-\infty}^{\infty} \mathrm{d}t \; \mathrm{e}^{-\cos^2\theta_i \, \mathrm{J}(t)} \mathrm{e}^{-\mathrm{i}(\epsilon_i \pm \tilde{\epsilon}_i)t} \mathrm{e}^{-\frac{\Gamma_{\mathrm{W}}(\epsilon_i \pm \tilde{\epsilon}_i)}{2}|t|} \tag{3.41}$$

$$\Gamma_{\mathrm{D},\pm}^i = \frac{\sin^2\theta_i}{4} \frac{\mathrm{J}(\epsilon_i \pm \tilde{\epsilon}_i)}{1 - \mathrm{e}^{-\beta(\epsilon_i \pm \tilde{\epsilon}_i)}} \tag{3.42}$$

and

$$\Gamma_{\mathrm{SF},\pm}^i = \Gamma_{\mathrm{D},\pm}^i + \Gamma_{\mathrm{F},\pm}^i \tag{3.43}$$

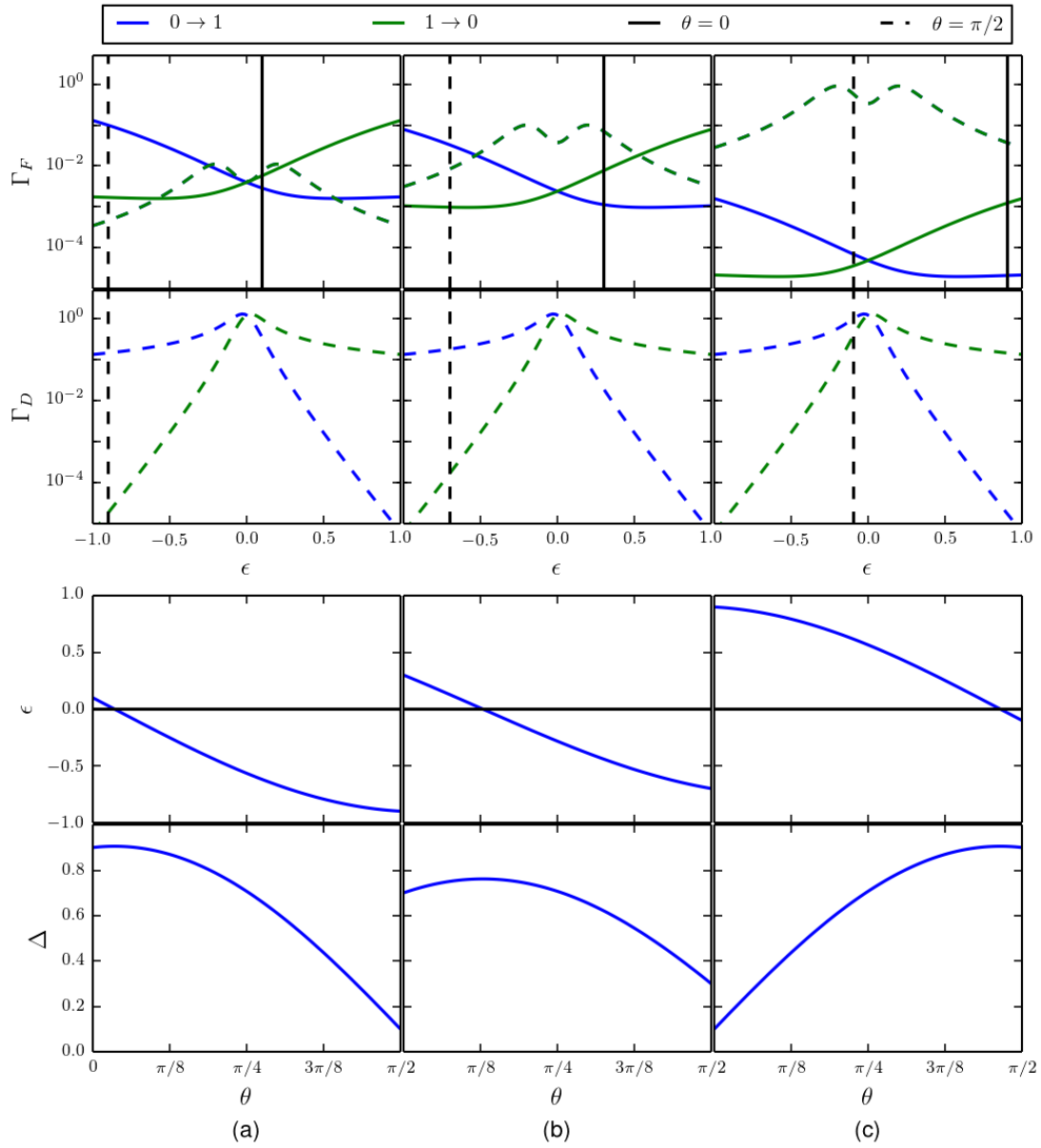


**Figure 3.5:** Comparison of the energy $\epsilon$ and tunneling amplitude $\Delta$ as a function of the rotation angle $\theta$ (bottom) and the flip and decay rate as a function of energy $\epsilon$ (top). In the rate plots the the blue (green) lines represent the case when the qubit is in state $|0\rangle$ ($|1\rangle$) at $\theta = 0$ (solid) and $\theta = \pi/2$ (dashed). The vertical lines in the rate plots give the energy at $\theta = 0$ and $\theta = \pi/2$ respectively. The three columns show different times at (a) the beginning of the schedule ($t/t_f = 0.1$) (b) near the jump in the $|1\rangle$ case ($t/t_f = 0.3$) and (c) at the end of the schedule ($t/t_f = 0.9$). Further parameters are $\beta = 10, \eta_{LF} = 5, \omega_{LF} = 0.1, \eta_{HF} = 0.5$, $\omega_{HF} = 10$ and, $h = 1$. The annealing schedule was assumed to be linear i. e. $\mathrm{A} = 1 - t/t_f$ and $\mathrm{B} = t/t_f$.

where the index $\pm$ distinguishes the two cases $J_{ij}\tilde{\tau}_z^j = \pm 1$.

Having determined the dynamics of single flip events let us now take a look at the double flip Hamiltonian $\mathcal{H}_{12}$, where both qubits decay simultaneously. Therefore we go back to Fermi's Golden rule

$$\Gamma_{\substack{1\to 0\\1\to 0}} = \sum_{i_B, f_B} \rho \int_{-\infty}^{\infty} \mathrm{d}t \ \langle i(t)|V|f(t)\rangle \langle f(0)|V|i(0)\rangle \tag{3.44}$$

and assume that both qubits are coupled to independent baths, i. e. $|i_B\rangle = |i_B^1\rangle |i_B^2\rangle$ and $\rho = \rho^1 \otimes \rho^2$. With this we get

$$\begin{aligned}\Gamma_{\substack{1\to 0\\1\to 0}} = \frac{M_{12}^2}{4} \int_{-\infty}^{\infty} \mathrm{d}t \ &\langle 1(t), 1(t)|\tau_x^1 \tau_x^2|0(t), 0(t)\rangle \\ &\times \prod_{i=1,2} \langle {U_-^i}^\dagger(t) U_+^i(t) {U_+^i}^\dagger(0) U_-^i(0)\rangle\end{aligned} \tag{3.45}$$

where we can recognize the bath correlator from the single qubit case and thus can recycle the result from Eqs. (3.17) and (3.21). To calculate the matrix element of the system states let us first have a look at the artificial case where only the first qubit evolves in time and the coupling constant is $J_{12} = +1$. With those assumptions the time evolution of the states are

$$|1(t), 1\rangle = \mathrm{e}^{\mathrm{i}(\epsilon_1 + \tilde{\epsilon}_1)\tau_z^1 t/2} |11\rangle = \mathrm{e}^{-\mathrm{i}(\epsilon_1 - \tilde{\epsilon}_1)t/2} |11\rangle \tag{3.46}$$

$$|0(t), 0\rangle = \mathrm{e}^{\mathrm{i}(\epsilon_1 + \tilde{\epsilon}_1)\tau_z^1 t/2} |00\rangle = \mathrm{e}^{+\mathrm{i}(\epsilon_1 + \tilde{\epsilon}_1)t/2} |00\rangle \tag{3.47}$$

and thus the matrix element becomes

$$\langle 1(t), 1|\tau_x^1 \tau_x^2|0(t), 0\rangle = \langle 11|\mathrm{e}^{-\mathrm{i}(\epsilon_1 + \tilde{\epsilon}_1)\tau_z^1 t/2} \tau_x^1 \tau_x^2 \mathrm{e}^{\mathrm{i}(\epsilon_1 + \tilde{\epsilon}_1)\tau_z^1 t/2}|00\rangle \tag{3.48}$$

$$= \mathrm{e}^{\mathrm{i}(\epsilon_1 - \tilde{\epsilon}_1)\tau_z^1 t/2} \mathrm{e}^{\mathrm{i}(\epsilon_1 + \tilde{\epsilon}_1)\tau_z^1 t/2} \tag{3.49}$$

$$= \mathrm{e}^{\mathrm{i}\epsilon_1 t}\,. \tag{3.50}$$

Here we can see that the term arising from the interaction between the two qubits cancels. This will also happen in the other cases. The only things that may change are the global sign in the exponent, by changing the state of the first qubit, or the sign in front of $\tilde{\epsilon}$, by changing the state of the second qubit or the coupling, in Eq. (3.49). Nevertheless the term arising from the coupling between the two qubits always cancels. This makes perfectly sense as the contribution of the interaction depends on the relative orientation between the to qubits. But when they flip simultaneously the relative orientation stays the same and thus its contribution cancels when taking the difference of the initial and final energy. Of course this behaviour changes if there are other spins coupling to the two flipping ones. Then those additional spins will have a contribution to the energy difference via the coupling term.

When we now enter the thoughts above in Eq. (3.45) the double flip rate becomes

$$\Gamma_{\mathrm{DF}} \equiv \Gamma_{\substack{1\to 0\\1\to 0}} = \frac{M_{12}^2}{4} \int_{-\infty}^{\infty} \mathrm{d}t \ \mathrm{e}^{-\mathrm{i}(\epsilon_1 + \epsilon_2)t} \mathrm{e}^{-(\cos^2\theta_1 + \cos^2\theta_2)\,\mathrm{J}(t)}\,. \tag{3.51}$$

This expression still lacks a line broadening we introduced in the single qubit case. So we repeat our magic trick and assume, because the two baths of the qubits are independent, that the line broadening

is simply given by the sum of the line broadening of both individual qubits. With this we get the final form for the double flip rate

$$\Gamma_{\mathrm{DF}} = \frac{M_{12}^2}{4} \int_{-\infty}^{\infty} \mathrm{d}t \; \mathrm{e}^{-(\cos^2\theta_1+\cos^2\theta_2)\,\mathrm{J}(t)} \mathrm{e}^{-\frac{1}{2}(\sin^2\theta_1\Gamma_{\mathrm{W}}^1+\sin^2\theta_2\Gamma_{\mathrm{W}}^2)|t|} \mathrm{e}^{-\mathrm{i}(\epsilon_1+\epsilon_2)t} \,. \tag{3.52}$$

Having determined the rates, let us now see how the rotation angle behaves, when we minimize the transition rate. Therefore we need the total transition rate given by

$$\Gamma_{\mathrm{tot}} = \Gamma_{\mathrm{SF}}^1 + \Gamma_{\mathrm{SF}}^2 + \Gamma_{\mathrm{DF}} \,. \tag{3.53}$$

Furthermore, as we are interested in the properties of an Ising spin glass used in [12], we set $h_1 = h_2 = 0$. All other parameters are kept the same as in Sec. 3.1.

In Fig. 3.6 the minimal angles $\theta_i^{\min}$ for all occurring cases are shown. The two cases when the state is $|01\rangle$ were omitted as they show exactly the same behaviour as Figs. 3.6c and (d) only the two angles $\theta_1^{\min}$ and $\theta_2^{\min}$ are swapped, which is nice as it shows us that it does not matter how we label our qubits. With the same effect the occurrence of the two global minima in Fig. 3.6a can be explained. The only difference here is that both qubits are in the same state and thus changing the labels at both qubits resolve to the same state. So two minima appear with the same, but swapped angles.

A precise description why the angles behave like this cannot be done unless an analytically solvable form of Eq. (3.53) or a way to visualize the numerical result is found. For this further investigation is needed. Nevertheless lets collect some observations. First of all the behavior is somewhat similar to the single qubit case. Meaning that at the beginning ($t/t_f = 0$) the angle starts at minimal energy $\epsilon_i + \tilde{\epsilon}_i$, i. e. at $\theta_i^{\min} = \pi/2$ if the qubit is in $|1\rangle$ or $\theta_i^{\min} = 0$ otherwise, and always becomes $\theta_i^{\min} = 0$ at the end ($t/t_f = 1$). Even during the annealing time ($0 < t/t_f < 1$) the angle prefers to be $\theta_i^{\min} \in \{0, \pi/2\}$. The only two exceptions where $\theta_i^{\min}$ also has other values than 0 and $\pi/2$ are the angles in Fig. 3.6a and $\theta_1^{\min}$ in Fig. 3.6d. These cases are also the only ones where at least one qubit is in state $|1\rangle$ and $J_{ij}\tilde{\tau}_z^i\tilde{\tau}_z^j = +1$. Furthermore one can see that the double flip rate $\Gamma_{\mathrm{DF}}$ can be neglected in most of the cases. Due to its prefactor $M_{12} \propto \sin\theta_1 \sin\theta_2$ it can only have values other than zero if and only if both angles are not zero. Thus only in Figs. 3.6a and (b) it can contribute.

Most of the weird behaviour has its origin in setting $h_i = 0$ and introducing the coupling between the qubits. By that the energy becomes

$$\epsilon_i + \tilde{\epsilon}_i = -\,\mathrm{A}\sin\theta_i + \mathrm{B}\cos\theta_i \cos\theta_j J_{ij}\tilde{\tau}_z^j \,. \tag{3.54}$$

This has some far-reaching consequences compared to the single qubit case. First of all the sign in front of the B-term, which was fixed in the single qubit case, now can vary depending on the sign of $J_{ij}\tilde{\tau}_z^j$. With this the qubits can now reach new energies. To visualize this new behaviour in Fig. 3.7 the possible energies were plotted above the single flip rate $\Gamma_{\mathrm{SF}}$ Eq. (3.34). This could be part to explain the linear decay of $\theta_1^{\min}$ in Fig. 3.6d as its energy corresponds to the dashed white line in Fig. 3.7. Furthermore by coupling the two qubits the second qubit can turn off the B-dependency completely, if $\theta_j^{\min} = \pi/2$, and thus pin the energy for $\theta_i^{\min} = 0$ to zero. Those changes are rather small but have a dubious impact. If we look at the jump in Fig. 3.6c for example. Here the jump happens at $\tau/t_f \approx 0.4$ so the energies right before the jump are given by $\epsilon_1 + \tilde{\epsilon}_1 = -\,\mathrm{A} \approx -0.6$ and $\epsilon_2 + \tilde{\epsilon}_2 = 0$ while directly after the jump they become $\epsilon_i + \tilde{\epsilon}_i = +B = 0.4$ for both qubits. So at the jump of the angle also the

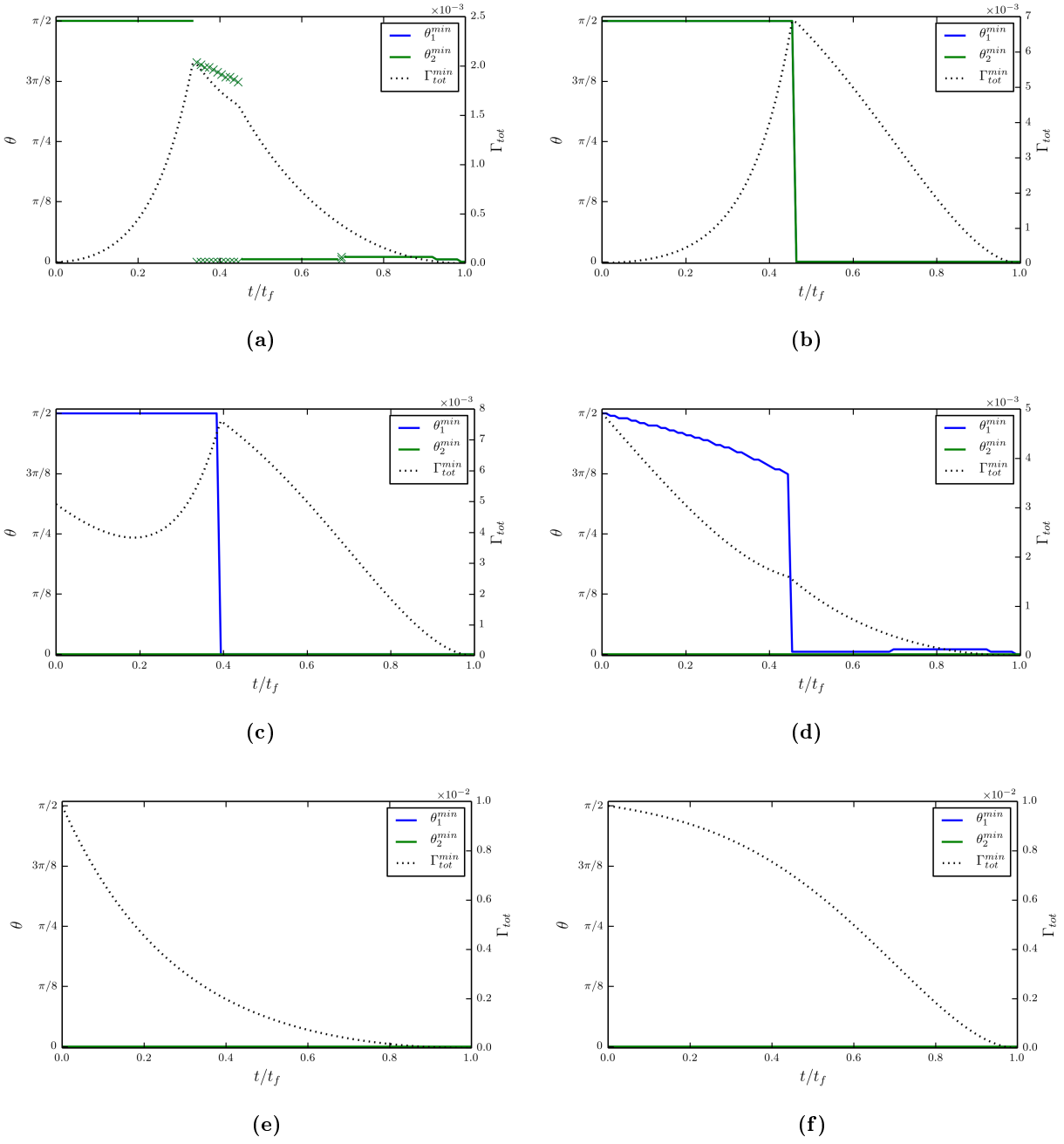


**Figure 3.6:** Plots of the minimal rate $\Gamma_{\text{tot}}^{\text{min}}$ and the corresponding angles $\theta_i^{\text{min}}$ when the system is in state (a) $|11\rangle$ with $J_{ij} = +1$, (b) $|11\rangle$ with $J_{ij} = -1$, (c) $|10\rangle$ with $J_{ij} = +1$, (d) $|10\rangle$ with $J_{ij} = -1$, (e) $|00\rangle$ with $J_{ij} = +1$, and (f) $|00\rangle$ with $J_{ij} = -1$. Using the parameters $\beta = 10, \eta_{LF} = 5, \omega_{LF} = 0.1, \eta_{HF} = 0.5$, $\omega_{HF} = 10$ and, $h_i = 0$ and a linear annealing schedule. The crosses in (a) show times where there was no unique minimum.

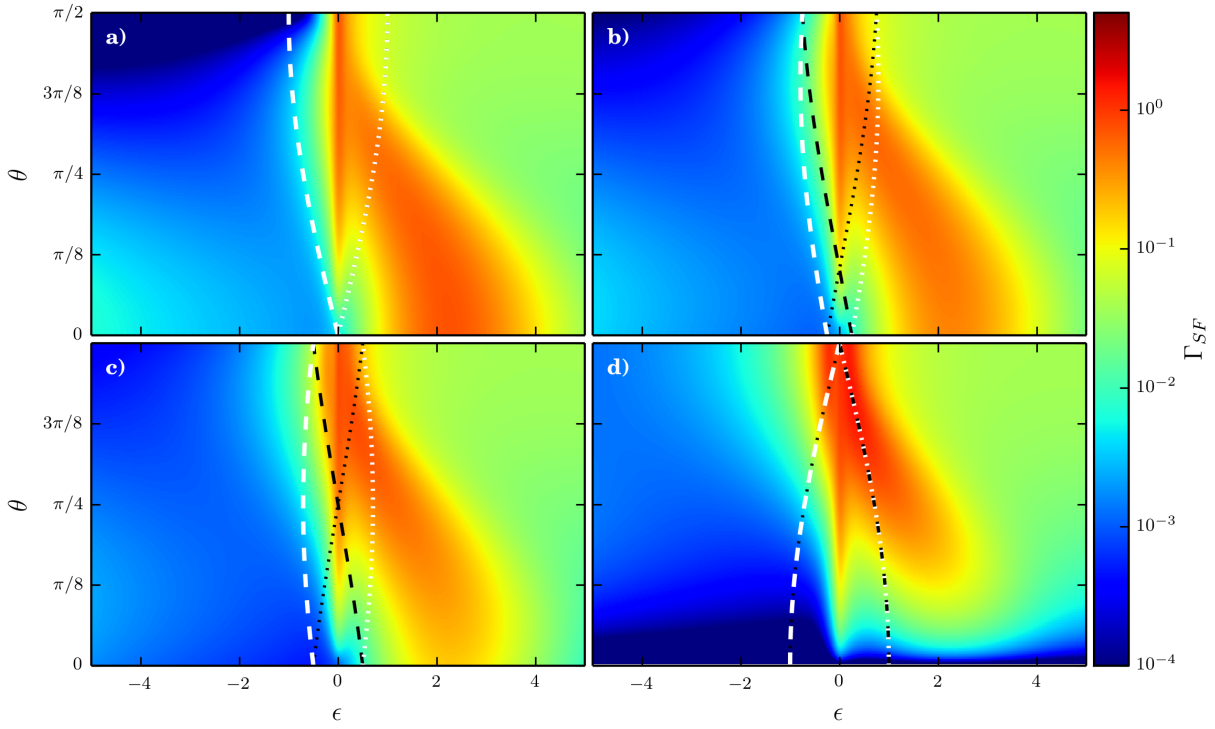


**Figure 3.7:** Plot of the single flip rate Eq. (3.34) as a function of $\epsilon$ and $\theta$ for a) $t/t_f = 0$, b) $t/t_f = 0.25$, c) $t/t_f = 0.5$ and d) $t/t_f = 1$ with parameters $\beta = 10, \eta_{LF} = 5, \omega_{LF} = 0.1, \eta_{HF} = 0.5, \omega_{HF} = 10$ and, $h = 1$ and assuming a linear annealing schedule i. e. $\mathrm{A} = 1 - t/t_f$ and $\mathrm{B} = t/t_f$. The black dashed (dotted) line is the energy $\pm(-\mathrm{A}\sin\theta + \mathrm{B}\cos\theta)$ and the white dashed (dotted) line the energy $\pm(-\mathrm{A}\sin\theta - \mathrm{B}\cos\theta)$ at the given time.

energy has an instantaneous and dramatic jump. It is needless to mention that this does not work very well with our assumption of an adiabatic environment.

But there is even more. By setting $h_i = 0$ and adding the interaction not only the energy but also the tunneling amplitude changes its behaviour and now becomes

$$\Delta_i + \tilde{\Delta}_i = \mathrm{A}\cos\theta_i + \mathrm{B}\sin\theta_i \cos\theta_j J_{ij}\tilde{\tau}_z^j \,. \tag{3.55}$$

So the tunneling amplitude, just as the energy, can flip the sign in front of the B-term as well as turn off the B-dependency completely. While changing the sign, if limited to $\theta_i^{\min} \in \{0, \pi/2\}$, does not have any influence as the tunneling amplitude only appears as square, turning off the the B-dependency has. Therefore let us have a look at Fig. 3.6b before the jump happens. Here both angles are $\theta_1^{\min} = \theta_2^{\min} = \pi/2$ so the tunneling amplitude becomes exactly zero and thus the flip rate has no influence at all. Furthermore when we look at the beginning of Fig. 3.6c where $\theta_1^{\min} = \pi/2$ and $\theta_2^{\min} = 0$ the tunneling amplitudes of both qubits show reverse behaviour, i. e. $\Delta_1 + \tilde{\Delta}_1 = \mathrm{B}$ while $\Delta_2 + \tilde{\Delta}_2 = \mathrm{A}$.

Finally let us have a look on the effect of the double flip on the behavior of the angles. As mentioned earlier only in Figs. 3.6a and (b) the double flip rate has values other than zero. For those two cases the minimal angles $\theta_i^{\min}$, ignoring the double flip rate $\Gamma_{\mathrm{DF}}$, are plotted in Fig. 3.8. In both cases the influence on the value of the total rate is rather small. But one can see, that in both cases the time

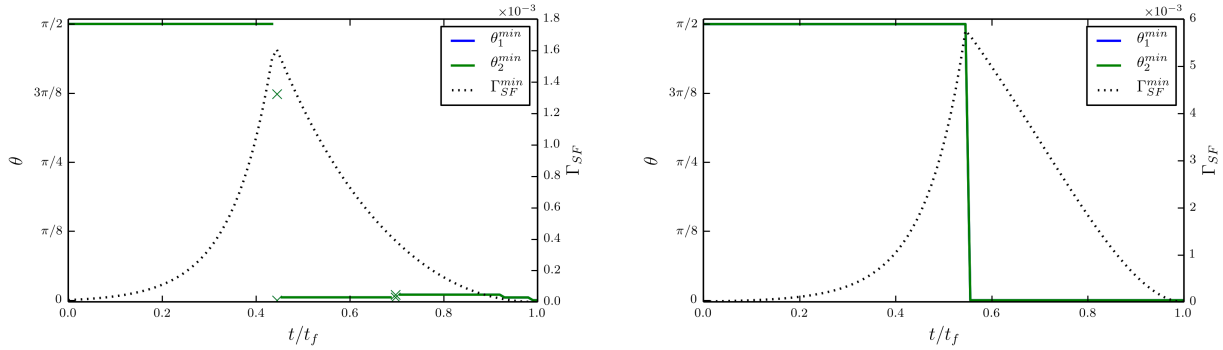


**(a)** **(b)**

**Figure 3.8:** Plots of the minimal rate $\Gamma_{\text{tot}}^{\min}$, ignoring the double flip rate $\Gamma_{\text{DF}}$, and the corresponding angles $\theta_i^{\min}$ when the system is in state (a) $|11\rangle$ with $J_{ij} = +1$, (b) $|11\rangle$ with $J_{ij} = -1$. Using the parameters $\beta = 10, \eta_{LF} = 5, \omega_{LF} = 0.1, \eta_{HF} = 0.5$, $\omega_{HF} = 10$ and, $h_i = 0$ and a linear annealing schedule. The crosses in (a) show times where there was no unique minimum.

in which $\theta_1^{\min} = \theta_2^{\min} = \pi/2$ is significantly shorter when considering the double flip rate. This makes perfectly sense as the double flip rate $\Gamma_{\text{DF}}$ has its global minimum at $\Gamma_{\text{DF}}(\theta_i = 0) = 0$ and some finite, positive value otherwise. Thus its impact can only be to drive the minimum of the total rate to its minimum, i. e. to $\theta = 0$. Furthermore one can see that in Fig. 3.8a the phase where there is no unique minimum (nearly) vanishes. Thus the ambiguity is a consequence of the double flip. The exact reason why this happens cannot be explained unless one finds a way to visualize Eq. (3.53) and thus further research is needed.

## 3.3 $N$ Qubits

Let us now generalize our model discussed in Secs. 3.1 and 3.2 for $N$ coupled qubits. The coupling constant between two qubits is denoted by $J_{ij}$. We allow the qubits to be (anti-) ferromagnetic $J_{ij} = \pm 1$ or not coupled $J_{ij} = 0$. Furthermore the coupling must be symmetric $J_{ij} = J_{ji}$, i. e. both qubits "see" the same coupling between each other, and the diagonal term must vanish $J_{ii} = 0$, i. e. the qubits are not coupled to themselves. With those assumptions the Hamiltonian in the interaction picture reads

$$\mathcal{H} = \sum_i \left( -\frac{\mathrm{A}(t)}{2}\sigma_x^i - \frac{\mathrm{B}(t)}{2}\left( h_i\sigma_z^i + \frac{1}{2}\sum_j J_{ij}\sigma_z^i\sigma_z^j \right) - \frac{1}{2}\sigma_z^i X_i(t) \right) \tag{3.56}$$

where the additional factor $1/2$ in front of the coupling term compensates double counting. When we now apply the basis transformation

$$\sigma_x^i \to \cos\theta_i\tau_x^i - \sin\theta_i\tau_z^i \tag{3.57a}$$

$$\sigma_z^i \to \sin\theta_i\tau_x^i + \cos\theta_i\tau_z^i\,. \tag{3.57b}$$

the Hamiltonian can be written

$$\mathcal{H} = \sum_i \mathcal{H}_i + \frac{1}{2}\sum_{ij}\mathcal{H}_{ij} \tag{3.58}$$

where $\mathcal{H}_i$ is the single flip Hamiltonian discussed in Sec. 3.1 and $\mathcal{H}_{ij}$ the double flip Hamiltonian discussed in Sec. 3.2, i. e.

$$\mathcal{H}_i = -\frac{\Delta_i + \tilde{\Delta}_i}{2}\tau_x^i - \frac{\epsilon_i + \tilde{\epsilon}_i}{2}\tau_z^i - \frac{1}{2}(\sin\theta_i\tau_x^i + \cos\theta_i\tau_z^i)X_i(t) \tag{3.59a}$$

$$\mathcal{H}_{ij} = -\frac{M_{ij}}{2}\tau_x^i\tau_x^j \tag{3.59b}$$

with

$$\epsilon_i = -\,\mathrm{A}(t)\sin\theta_i + h_i\,\mathrm{B}(t)\cos\theta_i \qquad \tilde{\epsilon}_i = \mathrm{B}(t)\sum_j J_{ij}\cos\theta_i\cos\theta_j\tau_z^j \tag{3.60a}$$

$$\Delta_i = \mathrm{A}(t)\cos\theta_i + h_i\,\mathrm{B}(t)\sin\theta_i \qquad \tilde{\Delta}_i = \mathrm{B}(t)\sum_j J_{ij}\sin\theta_i\cos\theta_j\tau_z^j \tag{3.60b}$$

$$M_{ij} = \mathrm{B}(t)J_{ij}\sin\theta_i\sin\theta_j\,. \tag{3.60c}$$

The dynamics resulting from the Hamiltonian Eq. (3.58) can be separated into two effects. On one hand there are single flip events originating from the single flip Hamiltonian $\mathcal{H}_i$. Their transition rates can be calculated analog to Sec. 3.1 and result to

$$\Gamma^l_{\mathrm{SF}} = \Gamma^l_{\mathrm{D}} + \Gamma^l_{\mathrm{F}} \tag{3.61}$$

where

$$\Gamma^l_{\mathrm{D}} = \frac{\sin^2\theta_l}{4}\frac{\mathrm{J}(\epsilon_l + \tilde{\epsilon}_l)}{1 - \mathrm{e}^{-\beta(\epsilon_l+\tilde{\epsilon}_l)}} \tag{3.62}$$

is the noise induced decay rate, with spectral function $\mathrm{J}(\epsilon)$, and

$$\Gamma^l_{\mathrm{F}} = \frac{(\Delta_l + \tilde{\Delta}_l)^2}{4}\int_{-\infty}^{\infty}\mathrm{d}t\;\mathrm{e}^{-\cos^2\theta_l\,\mathrm{J}(t)}\mathrm{e}^{-\frac{1}{2}\Gamma^l_{\mathrm{W}}|t|}\mathrm{e}^{-\mathrm{i}(\epsilon_l+\tilde{\epsilon}_l)t} \equiv \frac{(\Delta_l + \tilde{\Delta}_l)^2}{4}\int_{-\infty}^{\infty}\mathrm{d}t\;\gamma^l_{\mathrm{F}}(t) \tag{3.63}$$

is the system induced flip rate where

$$\Gamma^l_{\mathrm{W}} = \frac{\sin^2\theta_l}{8}\,\mathrm{J}(\epsilon_l + \tilde{\epsilon}_l)\coth\frac{\beta(\epsilon_l + \tilde{\epsilon}_l)}{2} \tag{3.64}$$

is the line broadening originating from the transverse coupling of the noise to the qubit. On the other hand there are double flip events originating from the double flip Hamiltonian, as its name suggests, flipping two qubits simultaneously. The transition rate to simultaneously flip the $l$-th and $m$-th qubit can be calculated analog to Sec. 3.2 and results to

$$\Gamma^{lm}_{\mathrm{DF}} = \frac{M^2_{lm}}{4}\int_{-\infty}^{\infty}\mathrm{d}t\;\gamma^l_{\mathrm{F}}\gamma^m_{\mathrm{F}}\mathrm{e}^{-2\mathrm{i}J_{lm}\sin\theta_l\sin\theta_m\tilde{\tau}^l_z\tilde{\tau}^m_z t} \tag{3.65}$$

where $\gamma_{\mathrm{F}}$ is the integrand of the flip rate in the single flip case. The extra factor in Eq. (3.65) compensates the loss of the coupling term of the two flipping qubits. This is necessary as the orientation of the two qubits, and with this the contribution to the energy, stays the same when both are flipped simultaneously.

# Chapter 4
# 4 Simulation

*In this chapter we report on the simulation we made with the goal to reproduce the result from [12] with our model. Therefore, we first introduce the Kinetic Monte Carlo Method in Sec. 4.1, which we used for the simulation. Then, in Sec. 4.2 we describe the deviations of the model used in the simulation from the model derived in Chap. 3. After that we discuss the implementation of the program used to do the simulation in Sec. 4.3. In this connection we concentrate on the methods we used to keep the computational complexity down and sketch the structure of the program only shortly. Finally, we present the results we obtain from the simulation in Sec. 4.4.*

## 4.1 The Kinetic Monte Carlo Method

The Kinetic Monte Carlo Method (KMC) is a numerical method to solve master equations [19]. In this field it competes against the widely-used Metropolis algorithm. Although both algorithms provide a numerical solution to master equations, the ideas behind them are rather different.

With the Metropolis, algorithm the trajectory of a system is given by configurations at equidistant time steps. At each step, the transitions from the given to a new configuration are considered. Those transitions are accepted with the probability given by the corresponding transition rate. But that also means that transitions can be rejected and thus there is a probability to have the same configuration at two succeeding steps. This probability increases when the transition rates decrease such that many failed tries are needed till a transition is accepted and thus slows down the algorithm.

In contrast to the Metropolis algorithm, the KMC algorithm is based on a waiting time image, i. e. the trajectory is built up by assigning a waiting time $\tau$ to the initial configuration of the system. After waiting, the system is ensured to make the transition to a new configuration, where the transition that is executed is chosen with the probability given by the corresponding transition rate. Then a new waiting time $\tau'$ is assigned to the new configuration and the whole procedure repeats. The difference to the Metropolis algorithm is that the waiting time $\tau$ is not constant but a random function of the transition rates. Therefore, at every time step a probability distribution of the waiting time is constructed such that no rejection occurs. By this, the waiting time increases when the transition rates decreases. Thus, in the regime of small transition rates, only few steps have to be executed, making the algorithm very efficient.

The procedure of the KMC has its downside when the transition rates are time-dependent. In this case the Metropolis algorithm can easily be expanded by assuming the transition rates to be piecewise constant on the interval $\Delta t$ between two steps, where the error made by this assumption becomes

smaller for smaller $\Delta t$. For the KMC this method does not work as the waiting time is an unbounded random function. With this, the transition rates between the arrival and departure in one state can differ, and thus the transition rates can not be assumed to be constant throughout the waiting time. So the distribution of waiting times has to be chosen with care such that it considers the time evolution of the transition rates.

### 4.1.1 Determination of the waiting time distribution

To determine the waiting time distribution, let us assume that the considered system has a discrete range of states. Then its dynamics is described by the master equation

$$\dot{p}_i(t) = \sum_j \Big( \Gamma_{j\to i}(t) p_j(t) - \Gamma_{i\to j}(t) p_i(t) \Big) \tag{4.1}$$

with time-dependent probabilities $p_i(t)$ to find the system in state $i$, and transition rates $\Gamma_{i\to j}(t)$ from state $i$ to $j$. Furthermore, let us define the total transition rate for leaving state $i$

$$\Omega_i(t) = \sum_j \Gamma_{i\to j}(t)\,. \tag{4.2}$$

To calculate the waiting time, we now consider the system to be in state $i$ at a given time $t$. Then $q_i(t+\tau|t)$ gives the probability for the system to stay in state $i$ after waiting for the time $\tau$, i. e. that no transition has taken place. Its time dependence can directly be taken from Eq. (4.1) and is given by

$$\dot{q}_i(t+\tau|t) = -\Omega_i(t+\tau) q_i(t+\tau|t)\,. \tag{4.3}$$

This equation can directly be integrated and leads, with starting condition $q_i(t|t) = 1$, to

$$q_i(t+\tau|t) = \exp\left[ -\int_t^{t+\tau} \mathrm{d}t'\; \Omega_i(t') \right]\,. \tag{4.4}$$

At this point, it is useful to define the dimensionless time scales

$$s_i = \int_0^t \mathrm{d}t'\; \Omega_i(t')\,, \tag{4.5}$$

where the index $i$ again denotes all possible states of the system. The different time scales for each state are necessary as, in general, each state has different escape channels and, by that, is associated with different total rates. For physical systems the transition rates have a real, positive and finite value. Thus, we can define an upper bound for the dimensionless time scale

$$s_i^{(\infty)} \equiv \lim_{t\to\infty} s_i = \lim_{t\to\infty} \int_0^t \mathrm{d}t'\; \Omega_i(t')\,. \tag{4.6}$$

Now recall that we are interested in the trajectory the system takes during time evolution. So the result can only be without ambiguity if the trajectory leads to a state in which the system will

remain frozen, i. e. for which the waiting time is infinite. In Eq. (4.4), we have already calculated the probability that no transition takes place in a time interval from $t$ to $t+\tau$. When we now assume that the system, at $t = 0$, is initiated in state $i$, then

$$q_i^*(0) \equiv \lim_{\tau\to\infty} q_i(\tau|0) = \lim_{\tau\to\infty} \exp\left[-\int_0^\tau \mathrm{d}t'\, \Omega_i(t')\right] = \mathrm{e}^{-s_i^{(\infty)}} \tag{4.7}$$

gives the probability of the system being frozen forever in state $i$. From this, we can also see that the system can only then be frozen in state $i$ if $s_i^{(\infty)}$ is finite. Thus the transition rates must fulfill the condition

$$\lim_{t\to\infty} t\Omega_i(t) = 0\,. \tag{4.8}$$

In general, the transition rates depend on the given state. Thus, in general, not all states satisfy Eq. (4.8) but only a certain subset of states. This does not pose a problem as long as there is at least one state that can get frozen. Otherwise the simulation has no unambiguous result.

Similarly, we can consider the case when the system arrives in state $i$ after a certain time $t$. Then the probability to become frozen in state $i$ can be calculated analog to Eq. (4.7) and reads

$$q_i^*(s_i) = \lim_{\tau\to\infty} q_i(t+\tau|t) = \mathrm{e}^{-(s_i^{(\infty)}-s_i)}\,. \tag{4.9}$$

Again the system can only become frozen if $s_i^{(\infty)}$ is finite and thus Eq. (4.8) holds for the transition rates. From Eq. (4.9), we can also conclude that, if $s_i^{(\infty)}$ is finite, the probability to become frozen grows with time and even becomes unity in the limit $t \to \infty$ as

$$\lim_{t\to\infty} q_i^*(s_i) = \lim_{t\to\infty} \mathrm{e}^{-(s_i^{(\infty)}-s_i)} = \mathrm{e}^{-(s_i^{(\infty)}-s_i^{(\infty)})} = 1\,. \tag{4.10}$$

This is a direct consequence of the condition for the transition rates in Eq. (4.8), which states that the total transition rate $\Omega_i(t)$ must go to zero for $t \to \infty$. Thus, for increasing time, the probability that the system undergoes a transition decreases.

Consequently, the waiting time for the system to be in state $i$ after arriving there at time $t$, including the possibility of the state to become frozen, can be generated the following way. Take a random number $u$ uniformly distributed in the interval $(0, 1]$. If $u < q_i^*(s_i)$ the system becomes frozen in state $i$. Otherwise wait for time $\tau$ such that $u = q(t+\tau|t)$. Usually it is more useful to invert Eq. (4.9) and write the condition in a slightly different but equivalent form. Then the procedure reads.

- Take a uniformly distributed random number $u \in (0, 1]$.
  - If
    $$-\ln u > s_i^{(\infty)} - s_i(t) \tag{4.11}$$
    the system becomes frozen in state $i$.
  - Otherwise, if
    $$-\ln u \le s_i^{(\infty)} - s_i(t)\,, \tag{4.12}$$

the system stays in state $i$ for the waiting time $\tau$, determined by

$$-\ln u = s_i(t+\tau) - s_i(t) = \int_t^{t+\tau} \mathrm{d}t'\, \Omega_i(t')\,, \tag{4.13}$$

before it makes the transition to state $j$ determined by the transition rates $\Gamma_{i\to j}$.

Although Eq. (4.8) requires the total transition rates to be time-dependent, it can often be assumed to be constant during the waiting time. In this case te integral in Eq. (4.13) can be solved directly, leading to

$$\tau = -\frac{\ln u}{\Omega_i}\,. \tag{4.14}$$

When this assumption can be made, the method is called the time-independent Kinetic Mote Carlo.

### 4.1.2 Numerical calculation of the waiting time

Although the condition that determines the waiting time, Eq. (4.13), looks simple the calculation of it in practice is quite complicated and can only be done analytically for transition rates with a simple structure. But there is an accurate approximation that can be used without increasing the computational complexity too much. This approximation is, similar to the Metropolis algorithm, based on the discretization of time in intervals $I_n$ with a fixed length $\Delta t$

$$I_n = [t_{n-1}, t_n) \tag{4.15}$$

where $t_n = n\Delta t$ with $n \in \mathbb{N}$. Therefore, the interval length $\Delta t$ has to be chosen in such a way that the transition rates $\Omega_i$ can be approximated as constants in each of the intervals, i. e. the condition

$$\partial_t \Omega_i(t)\Delta t \ll \Omega_i(t) \tag{4.16}$$

must hold. With this we can assign the constant value

$$\Omega_i^n \equiv \Omega_i(t_n) \tag{4.17}$$

to the total transition rates in the respective interval $I_n$. Note that $\Omega_i^n$ can also be defined differently, e. g. at the center of the interval or as mean value of the rates. When condition Eq. (4.16) is fulfilled, the different definitions only have a negligible influence on the value and even coincide in the limit $\Delta t \to 0$.

With the definitions above, we can now discretize the integral in Eq. (4.13). To this end, let us assume that $t \in I_n$. Then, there are two possibilities either the upper limit is in the same interval or it is not. If $t + \tau \in I_n$ the integral can easily be solved as the transition rate is constant on the interval,

$$\int_t^{t+\tau} \mathrm{d}t'\, \Omega_i(t') = \tau\Omega_i^n\,, \tag{4.18}$$

and thus

$$\tau = -\frac{\ln u}{\Omega_i^n}\,. \tag{4.19}$$

In the other case, when $t+\tau \notin I_n$, we split the integral and get

$$\int_t^{t+\tau} \mathrm{d}t'\ \Omega_i(t') = (t_n - t)\Omega_i^n + \int_{t_n}^{t+\tau} \mathrm{d}t'\ \Omega_i(t') \tag{4.20}$$

where the first term on the RHS is the area in interval $I_n$ and the second is the excess area outside $I_n$. The same procedure can then be applied to the integral in the second term until we reach interval $I_l$ with $t+\tau \in I_l$ and thus have split the integral into a sum of rectangles.

This directly suggests an iterative method to calculate the waiting time. As before, let us assume that we arrived in state $i$ at a time $t$. Then we define a waiting time

$$\tau_0 = -\frac{\ln u}{\Omega_i^n}\,. \tag{4.21}$$

If $\tau_0 < t_n - t$, it follows that $\tau_0 + t \in I_n$, and thus that the waiting time is given by $\tau = \tau_0$. Otherwise, area exceeding interval $I_n$ is given by $(\tau_0 - (t_n - t))\Omega_i^n$, and thus the length of the rectangle in the next interval is

$$u_1 = (\tau_0 - (t_n - t))\frac{\Omega_i^n}{\Omega_i^{n+1}}\,. \tag{4.22}$$

Using this, we can define a new waiting time

$$\tau_1 = u_1 + (t_n - t) = (\tau_0 - (t_n - t))\frac{\Omega_i^n}{\Omega_i^{n+1}} + (t_n - t)\,. \tag{4.23}$$

If now $\tau_1 < t_{n+1} - t$ the waiting time is given by $\tau = \tau_1$. Otherwise the length in the next interval is given by

$$u_2 = (\tau_1 - (t_{n+1} - t))\frac{\Omega_i^{n+1}}{\Omega_i^{n+2}}\,, \tag{4.24}$$

and with that the waiting time is

$$\begin{aligned}\tau_2 &= u_2 + \Delta t + (t_n - t)\\ &= u_2 + (t_{n+1} - t)\\ &= (\tau_1 - (t_{n+1} - t))\frac{\Omega_i^{n+1}}{\Omega_i^{n+2}} + (t_{n+1} - t)\,.\end{aligned} \tag{4.25}$$

If now $\tau_2 < t_{n+2} - t$ the waiting time is given by $\tau = \tau_2$. Otherwise, this procedure is repeated until it reaches $\tau_l < t_{n+l} - t$ where

$$\tau_l = (\tau_{l-1} - (t_{n+l} - t))\frac{\Omega_i^{n+l-1}}{\Omega_i^{n+l}} + (t_{n+l-1} - t) \tag{4.26}$$

and the waiting time is given by $\tau = \tau_l$. A simple example of this procedure is given in Fig. 4.1. In this example the rescaling procedure to the next interval is needed.

In the previous discussion, we have always assumed that there is a $\tau_l$ with $\tau_l < t_{n+l} - t$. Of course, this is not the case when the system gets frozen in state $i$. In this case, there is no such limit, and

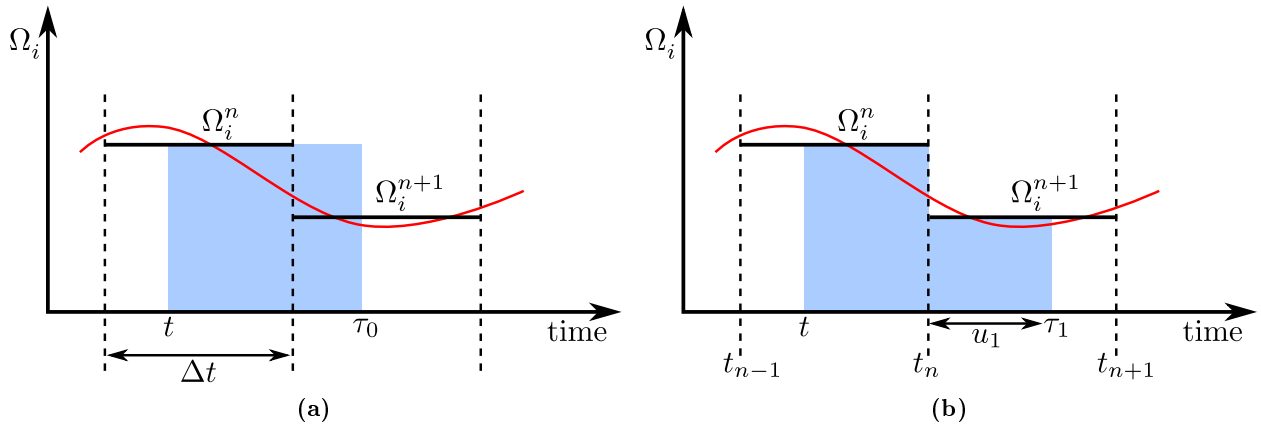


**Figure 4.1:** Example of a waiting time assignment in which the rescaling procedure is needed. The red line indicates the total transition rate $\Omega_i$ and the black lines give its approximated constant values $\Omega_i^n$ ($\Omega_i^{n+1}$) in interval $I_n$ ($I_{n+1}$). The blue shaded areas are both equal to the given value of the integral i. e. $-\ln u$. In part (a) the value of $\tau_0$ is given by Eq. (4.21). As it lies in interval $I_{n+1}$ the rescaling procedure is needed. The Area of the integral in $I_n$ is then given by $(t_n - t)\Omega_i^n$ and the excess area is $(\tau_0 - (t_n - t))\Omega_i^n$. In part (b) the quantity $u_1$ is the length of the basis of the rectangle with the same area as the excess area. Thus $\tau_1$ is given by the sum of the basis length of the rectangles from both $I_n$ and $I_{n+1}$ i. e. $\tau_1 = u_1 + (t_n - t)$. As $\tau_1$ is smaller than $t_{n+1}$ the iteration would have stopped and the waiting time would be given by $\tau_1$.

the evaluation would run up to the limit $l \to \infty$ which would be very costly in computation time. Therefore, it is more efficient to define a maximal simulation time $t_f$ and stop the simulation once $t + \tau_l > t_f$. Then, the system is assumed to be frozen in the state it had at time $t$. In doing so we introduce an additional error, as the state the system is frozen in does not have to be the state the system would have been frozen in in the limit $t \to \infty$. But if $t_f$ is chosen the way that $\Omega_i(t_f) \approx 0$ for all possible states $i$, the error made is small and can be neglected.

### 4.1.3 The Kinetic Monte Carlo Algorithm

The discussion from Secs. 4.1.1 and 4.1.2 leads to the following algorithm:

1. At time $t = 0$, initiate a state $i$ according to the initial probability distribution $p_i(0)$.
2. Set up a list of all possible transitions in state $i$.
3. Calculate the cumulative transition rates $R_n(t) = \sum_j^n \Gamma_{i\to j}(t)$, where $n = 1, 2, \ldots, N$ and $N$ is the total number of transitions from state $i$. In this notation $R_N = \Omega_i$.
4. Calculate the waiting time $\tau$ with

$$-\ln u = \int_t^{t+\tau} \mathrm{d}t'\, R_N(t')\,, \tag{4.27}$$

e. g. by using the method introduced in Sec. 4.1.2. Here, $u$ is a random number with $u \in (0, 1]$.

5. If $t + \tau > t_f$ stop the simulation. Otherwise:
   - Take a new random number $u' \in (0, 1]$.
   - Carry out event $n$ where $R_{n-1}(t + \tau) < u' R_N(t + \tau) \leq R_n(t + \tau)$.
   - Update the time to $t + \tau$.
   - Go back to step 2.

In general, the algorithm can have a big speed up by bookkeeping. For example, the transition rates usually depend on the energy difference between the states $i$ and $j$. If there are several states $j$ that have the same energy difference towards state $i$, then the transition rate only has to be calculated once per time step and then can be assigned to all transitions with the same energy difference. Unfortunately, there is no general way to do the bookkeeping but one has to review each given physical problem individually.

## 4.2 Model

For the simulation the model we use differs slightly from the model described in Chap. 3. This has two reasons. On the one hand the model was developed while doing the simulation, before growing complexity forced us to go back to the smaller toy models described in Chap. 3. On the other hand the simulation is very costly in computation time. Thus, some assumptions had to be made to keep the computation time down.

For the simulation, we assume that the control knobs $\{h_i\} = 0$ for all qubits. By this, the energy in $\sigma_z$-basis is only given by the coupling between the qubits. Furthermore, the exact time dependence for the rotation angles $\{\theta_i\}$ is unknown. Thus, we assume that the basis of all qubits is rotated by the same angle $\{\theta_i\} = \theta(t)$. For this common rotation angle we use two models for the time dependency. In the first model, we assume that the environment only couples weakly, such that system Hamiltonian dominates. Thus the state is given in the $\tau_z$-basis and is initiated in the ground state, i. e. all qubits are in state $|0\rangle$. In this model, the we assume the rotation angle to behave linear in time, i. e.

$$\theta(t) = \frac{\pi}{2}\left(1 - \frac{t}{t_f}\right) . \tag{4.28}$$

In the other model we assume that the coupling to the environment dominates the total Hamiltonian. This means that the qubits are in a $\sigma_z$-basis, corresponding to $\theta(t) = \text{const.} = 0$, throughout the simulation. From that also follows that the state at the beginning is not given by the ground state but is purely random.

Because the numerical integration of Eq. (3.63) and Eq. (3.65) would have been too costly in computation time for the simulation, we simplify the spectral function $\mathrm{J}(\omega)$ and ignore the broadband high-frequency part of it. By only considering the strongly peaked low-frequency part of the noise, we can now approximate the spectral function $\mathrm{J}(t)$ in Eq. (3.21), analog to [10], by expanding the exponent in it up to second order. By doing so the spectral function $\mathrm{J}(t)$ becomes

$$-\mathrm{J}(t) = -\int_{-\infty}^{\infty} \frac{\mathrm{d}\omega}{2\pi}\,\mathrm{S}(\omega)\frac{\mathrm{e}^{-\mathrm{i}\omega t} - 1}{\omega^2} \approx -\epsilon_\mathrm{p} t - \frac{W^2}{2}t^2 \tag{4.29}$$

with

$$\epsilon_{\mathrm{p}} = \mathcal{P} \int \mathrm{d}\omega \, \frac{\mathrm{S}(\omega)}{\omega} \tag{4.30a}$$

$$W^2 = \int \mathrm{d}\omega \, \mathrm{S}(\omega) \, . \tag{4.30b}$$

where $\mathcal{P}$ denotes principal value integration.

Inserting Eq. (4.29) into the flip rate Eq. (3.63), leads to

$$\Gamma_{\mathrm{F}}^{l} = \frac{(\Delta + \tilde{\Delta}_l)^2}{4} \int_{-\infty}^{\infty} \mathrm{d}t \, \mathrm{e}^{-\frac{\Gamma_{\mathrm{W}}^{l}}{2}|t|} \mathrm{e}^{-\frac{W^2 t^2}{2}\cos^2\theta} \mathrm{e}^{\mathrm{i}(\epsilon + \tilde{\epsilon}_l - \epsilon_{\mathrm{p}}\cos^2\theta)t} \, , \tag{4.31}$$

where we use the assumptions $\{\theta_i\} = \theta$ and $\{h_i\} = 0$ from above. Thus, the angle $\theta$, the energy $\epsilon$, and the tunneling amplitude $\Delta$ are now identical for all qubits and we can omit the index from now on. Now Eq. (4.31) can be solved analytically which leads to

$$\Gamma_{\mathrm{F}}^{l} = -\sqrt{\frac{\pi}{8}} \frac{(\Delta + \tilde{\Delta}_l)^2}{W\cos\theta} \, \mathrm{Re}\left( (\mathrm{erf}(x) - 1)\mathrm{e}^{x^2} \right) \, , \tag{4.32a}$$

where

$$x = \frac{\sqrt{2}\left( \Gamma_{\mathrm{W}}^{l} + 2\mathrm{i}(\epsilon + \tilde{\epsilon}_l - \epsilon_{\mathrm{p}}\cos^2\theta) \right)}{4W\cos\theta} \, . \tag{4.32b}$$

At this point, we can also see the meaning of $\epsilon_{\mathrm{p}}$ and $W$ from Eq. (4.30). When we go to the original basis, i. e. set $\theta(t) = 0$, the line broadening $\Gamma_{\mathrm{W}}^{l}$ vanishes and Eq. (4.32) simplifies to a Gaussian lineshape

$$\Gamma_{\mathrm{F}}^{l} = \sqrt{\frac{\pi}{8}} \frac{\Delta^2}{W} \exp\left[ \frac{(\tilde{\epsilon}_l - \epsilon_{\mathrm{p}})^2}{2W^2} \right] \, . \tag{4.33}$$

which allows us to identify $\epsilon_{\mathrm{p}}$ with a noise-induced energy offset and $W$ with a noise-induced resonance width.

Analog to the flip rate, the double-flip rate ,Eq. (3.65), can be approximated yielding to

$$\Gamma_{\mathrm{DF}}^{lm} = \frac{M_{lm}^2}{4} \int_{-\infty}^{\infty} \mathrm{d}t \, \mathrm{e}^{-\frac{1}{2}(\Gamma_{\mathrm{W}}^{l} + \Gamma_{\mathrm{W}}^{m})|t|} \mathrm{e}^{-W^2 t^2 \cos^2\theta} \mathrm{e}^{\mathrm{i}(\epsilon_{lm} - 2\epsilon_{\mathrm{p}}\cos^2\theta)t} \tag{4.34a}$$

where

$$\epsilon_{lm} = 2\epsilon + \tilde{\epsilon}_l + \tilde{\epsilon}_m - 2\sin^2\theta J_{lm} \tilde{\tau}_z^{l} \tilde{\tau}_z^{m} \tag{4.34b}$$

is the total energy difference between the initial and final state. This integral has the same structure like the one of the flip rate, and thus can be performed straightforwardly, leading to

$$\Gamma_{\mathrm{DF}}^{lm} = -\frac{\sqrt{\pi} M_{lm}^2}{4W\cos\theta} \, \mathrm{Re}\left( (\mathrm{erf}(x) - 1)\mathrm{e}^{x^2} \right) \, , \tag{4.35}$$

where

$$x = \frac{\Gamma_{\mathrm{W}}^{l} + \Gamma_{\mathrm{W}}^{m} + 2\mathrm{i}\left( \epsilon_{lm} - 2\epsilon_{\mathrm{p}}\cos^2\theta \right)}{4W\cos\theta} \, . \tag{4.36}$$

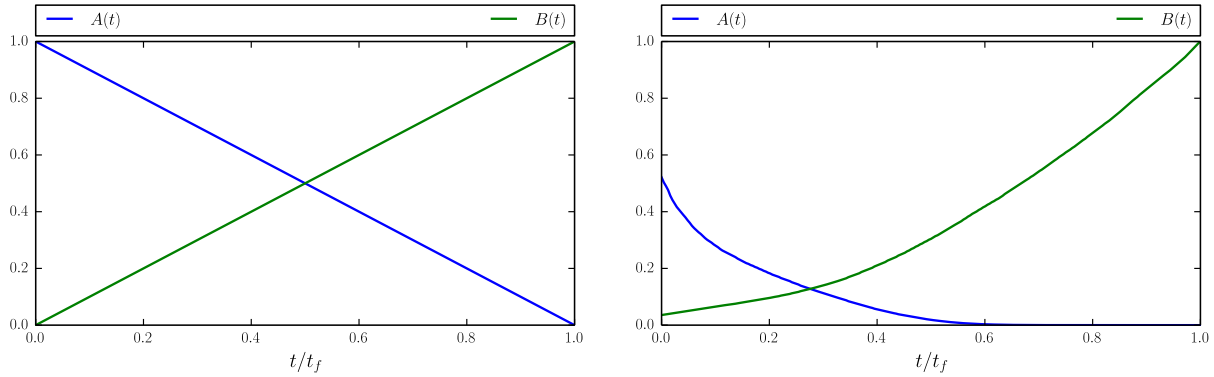


**(a)** **(b)**

**Figure 4.2:** Illustrations of the annealing schedules used in the simulation. Plot (a) shows the idealized linear schedule and (b) the one measured in a D-Wave One.

The structure of the decay rate Eq. (3.62) and the line broadening Eq. (3.64) does not change. But by applying the new assumptions they now read

$$\Gamma^l_{\mathrm{D}} = \frac{\sin^2\theta}{4} \frac{\mathrm{J}(\epsilon + \tilde{\epsilon}_l)}{1 - \mathrm{e}^{-\beta(\epsilon+\tilde{\epsilon}_l)}} \tag{4.37}$$

$$\Gamma^l_{\mathrm{W}} = \frac{\sin^2\theta}{8} \mathrm{J}(\epsilon + \tilde{\epsilon}_l) \coth \frac{\beta(\epsilon + \tilde{\epsilon}_l)}{2} \,. \tag{4.38}$$

In addition to the restricting changes from above, we extend the model used in the simulation. This means that, in addition to the linear annealing schedule

$$\mathrm{A}(t) = 1 - \frac{t}{t_f} \quad \text{and} \quad \mathrm{B}(t) = \frac{t}{t_f} \,, \tag{4.39}$$

used in Chap. 3, we also consider one measured in the D-Wave One [20]. Both schedules are illustrated in Fig. 4.2. Furthermore, we add a classical annealing phase at the end of the annealing schedule. This is justified since, at the end of the annealing schedule, the tunneling amplitude $\Delta \approx \mathrm{A} \to 0$ and thus the flip rate $\Gamma_{\mathrm{F}}$ is small, but at the same time we still have a finite temperature in the system. Therefore, at the end, the thermal excitations dominate and thus the annealing behaves classical. In this case, we propose the transition rates to be given by

$$\Gamma^l_{\mathrm{CA}} = 1 - \frac{1}{\mathrm{e}^{\beta\epsilon_l} + 1} \,, \tag{4.40}$$

i. e. the probability that an energy eigenstate is un-occupied in the Fermi-Dirac statistics.

## 4.3 Implementation

At the end of Sec. 4.1 it was already mentioned that the KMC algorithm can have a major speed up by bookkeeping. In this section we now present the methods used for our model to keep the computational cost down. First, we concentrate on the simplest case, when we are in the original basis throughout the

annealing schedule, i. e. when $\theta(t) = 0$. In this case, the transition rates are given by Eq. (4.33), where the only quantity that is not-identical for all qubit is the energy contribution from the interaction term, i. e.

$$\tilde{\epsilon}_l = \mathrm{B}(t) \sum_j J_{lj} \tilde{\tau}_z^l \tilde{\tau}_z^j \,. \tag{4.41}$$

In this expression the parameter $\mathrm{B}(t)$, from the annealing schedule, again is identical for all qubits. Thus we define a simulation energy

$$E_l = \sum_j J_{lj} \tilde{\tau}_z^l \tilde{\tau}_z^j \tag{4.42}$$

for each qubit.[1] But this simulation energy only has a limited range of possible values. By limiting the coupling to $J_{ij} = \pm 1$ and having eigenvalues $\tilde{\tau}_z^i = \pm 1$ we know, that the simulation energy must be an integer, i. e. $E \in \mathbb{Z}$. Furthermore, from the structure of the chip used in the D-Wave One and discussed in Sec. 2.2, we know that each qubit can only be coupled to a maximum of $N_{\text{links}}^{\max} = 6$ other qubits. Thus, the simulation energy must be in $E_l \in [-6, 6]$. When we combine both facts, we get that the simulation energy can have a maximum of $2N_{\text{links}}^{\max} + 1 = 13$ values. But from this follows, as the simulation energy is the only non-identical value in the transition rate, that there are only 13 different values for the transition rates per time step. So in a worst case scenario, only 13 values have to be calculated. Then those values only have to be assigned to the qubits with the corresponding simulation energy. Doing this one can expect a major speed up compared to the straightforward solution, where one calculates the transition rate individually for each of the $N = 108$ qubits per time step.

Another way to safe computation time is at the calculation of the simulation energy itself. Within the KMC the system transfers into a new state, defined by the transition rates, at every time step. Applied to our model, for $\theta(t) = 0$, that means that at each time step one of the qubits is flipped, as we have only defined single-flip rates in this case. Therefore at every step only the qubit that is flipped and the ones coupled to it change their energy, while for all other qubits it stays the same. Hence one can save computation time by computing the simulation energy once at the beginning of the simulation and then only updating the energy during the simulation for the qubits for which it has changed. This method is very efficient as these updates are easy to compute. For the flipping qubit we find

$$E_l' = \sum_j J_{lj} \tilde{\tau}_z^{l\prime} \tilde{\tau}_z^j = -E_l \,, \tag{4.43}$$

and for the coupled ones

$$E_j' = E_j - 2J_{lj} \tilde{\tau}_z^l \tilde{\tau}_z^j \,, \tag{4.44}$$

where the unprimed quantities are the ones before and, the primed ones after the transition. Thus, in worst case, one only has to make $N_{\text{links}}^{\max} + 1 = 7$ easy operations, change of one sign and add $\pm 2$, depending on the sign of $J_{lj} \tilde{\tau}_z^l \tilde{\tau}_z^j$, for every coupled qubit. Compared to the straightforward way, where the states are stored in a vector, and the coupling in a matrix, and the energy is obtained by matrix multiplication at every step, this method is expected to be way more efficient.

The final method to save computation time is directly connected with the calculation of the waiting time $\tau$ discussed in Sec. 4.1.2. In this method the time is divided into small intervals in which the transition rates can be approximated to be constant. Thus when using the time dependent version of

[1] Note that, as we defined our annealing schedule the way that $\mathrm{B}(t_f) = 1$, the simulation energy satisfies $E_l = \tilde{\epsilon}_l(t_f)$. Thus, $E_l$ also gives automatically the energy of the $l$-th qubit at the end of the annealing schedule. With this, the total energy is simply given by the sum over all simulation energies.

the KMC algorithm, we can assume the transition rates to be constant within one of those intervals. But when the transition rates can be assumed to be constant, they only have to be calculated once per interval. With this we get a speed up in the regime of large transition rates and thus small waiting times, since, in this regime, several simulation steps can lie within one interval.

The methods described above can, with some small changes, also be applied to the more general model when $\theta(t) \neq 0$. In this case, the single- and double-flip events have to be examined individually. First let us concentrate on the single-flip events. Here, the arguments with the transition rates being constant in a time interval and the way the simulation energy is computed and updated still hold and thus can directly be taken from the discussion above. Thus only the number of possible different transition rates and the way they are distinguished changes.

By allowing the rotation angle to have values $\theta(t) \neq 0$ our model now contains, in addition to the flip rate, a decay rate Eq. (4.37) and a line broadening Eq. (4.38). For both, with the assumptions made in Sec. 4.2, the only non-identical quantity is the qubit energy. Unfortunately, the energy now does not only has a contribution from the coupling but also one from the annealing schedule, i. e.

$$\epsilon + \tilde{\epsilon}_l = -\,\mathrm{A}(t)\sin\theta + \mathrm{B}(t)\cos^2\theta \sum_j J_{lj}\tilde{\tau}_z^j\,, \tag{4.45}$$

using the definitions from Sec. 3.3. Furthermore, at the derivation, we defined the decay rate to be

$$\Gamma^l_{1\to 0}(\epsilon + \tilde{\epsilon}_l) = \Gamma^l_{0\to 1}(-(\epsilon + \tilde{\epsilon}_l)) \equiv \Gamma^l_{\mathrm{D}}(\epsilon + \tilde{\epsilon}_l)\,, \tag{4.46}$$

which can be re-written, using the definition of the eigenvalues, i. e. $\tau_z\,|0\rangle = |0\rangle$ and $\tau_z\,|1\rangle = -\,|1\rangle$, yielding to

$$\Gamma^l_{\mathrm{D}}(\epsilon + \tilde{\epsilon}_l) = \Gamma^l_{\mathrm{D}}(-\tilde{\tau}^l_z(\epsilon + \tilde{\epsilon}_l))\,. \tag{4.47}$$

Inserting Eq. (4.45) into the argument of the RHS, we get the energy used in the calculation

$$-\,\tilde{\tau}^l_z(\epsilon + \tilde{\epsilon}_l) = \mathrm{A}(t)\sin\theta\tilde{\tau}^l_z - \mathrm{B}(t)\cos^2\theta\sum_j J_{lj}\tilde{\tau}^l_z\tilde{\tau}^j_z = \mathrm{A}(t)\sin\theta\tilde{\tau}^l_z - \mathrm{B}(t)\cos^2\theta E_l \tag{4.48}$$

where we used the definition of the simulation energy, Eq. (4.42), in the last step. Thus, in the general model when $\theta \neq 0$, the energy not only depends on the simulation energy but also on the state of the qubit itself. Hence we have $N_{\mathrm{E}} = 2(2N^{\max}_{\mathrm{links}} + 1) = 26$ possible different values for the energy and therefore also for the decay rate and the line broadening.

The same, but with a slightly different argument, holds for the flip rate. For the flip rate, the energy is not the only non-identical quantity, but it also depends on the contribution of the coupling to the tunneling amplitude

$$\tilde{\Delta}_l = \mathrm{B}(t)\sin\theta\cos\theta\sum_j J_{lj}\tilde{\tau}^j_z\,. \tag{4.49}$$

With a simple trick, we can bring this contribution in a form similar to the energy. To this end we multiply Eq. (4.49) by $\tilde{\tau}^{l2}_z = 1$, and get

$$\mathrm{B}(t)\sin\theta\cos\theta\sum_j J_{lj}\tilde{\tau}^j_z\tilde{\tau}^{l2}_z = \mathrm{B}(t)\sin\theta\cos\theta E_l\tilde{\tau}^l_z\,. \tag{4.50}$$

Thus, in order to determine the tunneling amplitude, the same cases as for the energy have to be distinguished. But from that also follows that the flip rate is determined by the same $N_{\mathrm{E}} = 26$ cases

like the decay rate and the line broadening. Hence, all single-flip events depend on the same 26 different cases and thus the same strategy as in the simple case can be used.

Having determined the methods for the single-flip events, let us now concentrate on the double-flip events, where things get kind of nasty. The double-flip events are fully described by the double-flip rate in Eq. (4.35). So let us take a look on the different components non-identical for all qubits. First of all there is the matrix element

$$M_{lm} = \mathrm{B}(t) J_{lm} \sin^2\theta \,. \tag{4.51}$$

Here only the coupling $J_{lm} = \pm 1$ is non-identical but as the matrix element only appears squared, the over-all factor $M_{lm}^2$ is again identical for all qubits. Next, there is the sum of the two line broadening terms. From the discussion above, we already know that each single line broadening depends on the energy, and thus can have $N_\mathrm{E} = 26$ different values. Furthermore, as we are interested in the sum, the order of the two term does not play a role. Therefore it is sufficient to compute pair of energies only once, e. g. the pairs $(1, 2)$ and $(2, 1)$ give the same result. Overall this gives $(N_\mathrm{E} + 1)N_\mathrm{E}/2 = 351$ different possible values for the sum of the two line broadening terms. Finally, there is the total energy difference $\epsilon_{lm}$, Eq. (4.34b). Luckily, the situation here is (almost) identical to the discussion for the two line broadening terms. The only difference is that next to the sum of both energies, for which the same arguments as above hold, there is the term to compensate the loss of the coupling between the two flipping qubits, which can have two different values, $J_{lm}\tilde{\tau}_z^l\tilde{\tau}_z^m = \pm 1$.[2] Altogether there are a total of $N_{\Gamma_\mathrm{DF}} = (N_\mathrm{E} + 1)N_\mathrm{E} = 702$ different possible values for the double-flip rate.

When we now, naively, compare the total number of possible values with $N = 108$, the number of qubits, we see that there are more possibilities than qubits, Therefore, naively, no speed up can be expected by doing the bookkeeping. However the the naive way does not describe the correctly. First of all the number of qubits is the wrong quantity to compare with. In contrast to the single-flip rate, the double-flip rate must be calculated for each coupling in the system, not for each qubit. Thus the quantity to compare with is the total number of couplings $N_\mathrm{links}^\mathrm{tot} = 255$ in the system.

Furthermore, the analysis above is a worst case scenario. The number of qubits coupled to each qubit, for example, has been assumed to be the maximum number $N_\mathrm{links}^\mathrm{max} = 6$, which is not true for most qubits, e. g. because they are at the edge of the chip or they are coupled to a broken or not used qubits. If we use the average $N_\mathrm{links}^\mathrm{av} = 4.7 \pm 1.2$ instead of the maximum number of couplings we get $N_{\Gamma_\mathrm{DF}}^\mathrm{av} \approx 450$ possibilities, a number much closer to the number of couplings. But this is still not the average situation we expect to happen in a simulation as it still assumes that the simulation energies are uniformly distributed over the possible values. However they are, especially at later times, cumulating at lower energies and thus reducing the number of possibilities further. Altogether we assume the bookkeeping, for double-flip events, to have a net speed up larger than the overhead needed to do the bookkeeping.

For the double-flip case, we also have to adjust the way the energies are updated. Here, we have to remember that the energy contribution by the coupling of the two flipping qubits stays the same before and after the flip. When we consider this, the new energy for the flipping qubits is given by

$$E_l' = -E_l + 2J_{lm}\tilde{\tau}_z^l\tilde{\tau}_z^m \,. \tag{4.52}$$

In the case of the qubits coupled to the flipping ones previous discussion still holds and we can use Eq. (4.44). Of course this cannot be done in general. But the structure of the chip used in the D-Wave

[2] Note that the different eigenvalues $\tilde{\tau}_z^{l/m}$ are already considered in the discussion for the energies. Thus it would be sufficient to only consider the coupling $J_{lm} = \pm 1$ to distinguish the extra cases. But as both, the coupling $J_{lm}$ and $J_{lm}\tilde{\tau}_z^l\tilde{\tau}_z^m$, can have two different values it does not make a difference which criteria we use to distinguish the two cases. So we choose $J_{lm}\tilde{\tau}_z^l\tilde{\tau}_z^m$ as it makes the implementation a little nicer.

One, as described in Sec. 2.2, prevents any qubit to be coupled to both flipping ones. Thus only the energy contribution from one coupling has to be considered when updating the energy of the coupled qubits.

The discussion above shows that there are two basic mechanisms to safe computation time. On the one hand by updating the energy and on the other hand by keeping track of the values of the transition rates that have already been computed. This directly suggests to base the simulation on two main classes, we call them `State` and `RateList`, each taking care of one of the mechanisms. For the implementation we use `C++`, in the `C++11` standard, as programming language.

Hereby, the main job of the class `State` is to hold and update all necessary information about the current state of the state, including to update the energy with the method described above. For this, it contains a `std::vector`, from the `C++` Standard Library, with one instance of `Site` per qubit. The `Site` class is used to store the internal id of the qubits used to access other information about the qubit not stored in `Site`, the current energy, and the links to other qubits, i. e. the information to which qubit with which coupling constant the qubit is coupled. This does not include the current state of the qubit. This information is moved to an extra class `SpinChain` which is based on an instance of `boost/dynamic_bitset` from the Boost libraries [21]. The main reason we do this is for convenience as the `boost/dynamic_bitset` allows bitwise operations, like `std::bitset`, which simplifies the random initiation, needed for the $\theta(t) = 0$ case, as well as setting the size at run time, like `std::vector<bool>`, which gives the flexibility to run systems with a different number of qubits without the need to recompile.

At initiation of the class `State` we make use of the helper class `Lattice`. The main job of class `Lattice`, besides initiating the class `State`, is to read the instance files [15], i. e. the files where the information about the coupling between the qubits is stored in, and to process the information to the form needed in the `State` class. We move the file operation out of the `State` class as for each run a new instance of `State` is needed. Thus, by moving the file operation into the class `Lattice`, we keep the number of file operations to a minimum, as then each instance file only has to be read once. In addition to this, the `State` class contains an extra `std::vector` storing all couplings existing in the system. This duplicate information about the coupling is stored, because it is most convenient when the information is provided differently for different situations. For computing and updating the energy, it is most convenient to have the information about the coupling for each single qubit individually. Therefore this information is stored in `Site`. But for double-flip events we need to compute the corresponding transition rate for each single coupling in the system. If the information was only stored in `Site` one would have to iterate through all instances of `Site`, and the couplings within, and exclude double-counting at every step. Therefore it is more efficient to "waste" some memory instead and store the information separately. With this, the iteration has to be done only once at initiation. For computing the double-flip rate, it is then sufficient to iterate once through this new `std::vector`.

The job of the second base class `RateList`is to compute the transition rates and to do the respective bookkeeping as described above. Therefore, the transition rates are defined as member functions of `RateList`. At initiation, a function pointer is set to the corresponding member function and accessed via the parenthesis operator. The parenthesis operator also takes care of the bookkeeping. To distinguish the cases described above, it is overloaded several times with the arguments needed to calculate the transition rates in the different cases. The information whether a given case has already been calculated is again stored in an instance of `boost/dynamic_bitset`, and the corresponding value in a `std::vector`. When the parenthesis operator is called, it first checks if the given case is already computed. If not, it computes the value, stores it in the `std::vector` and returns it otherwise it simply returns

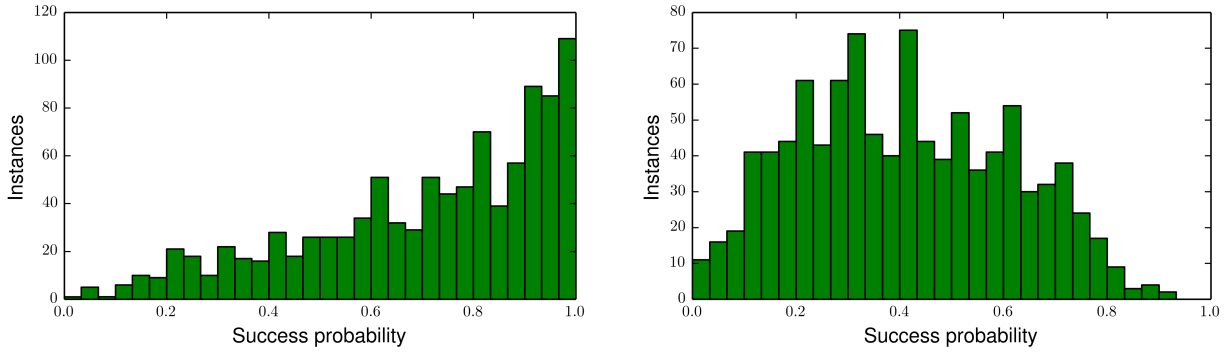


(a) (b)

**Figure 4.3:** Histogram of the probabilities of finding the ground state of 1000 different spin glass instances with $N = 108$ spins for strong coupling to the environment, i. e. $\theta(t) = 0$. For the simulation we use the time-independent KMC, a temperature of $k_B T = 0.1$, and (a) the linear and (b) the measured annealing schedule. Both plots show a unimodal distribution of the success probabilities.

the corresponding value from the `std::vector`. At the beginning of each step or every time the simulation leaves one time interval, if using the time-dependent version of KMC described in Sec. 4.1, the `boost/dynamic_bitset` is reset, i. e. all elements set to `false`. At this point, the time-dependent parameters, i. e. the parameters of the annealing schedule $\mathrm{A}(t)$ and $\mathrm{B}(t)$, and the rotation angle $\theta(t)$, are updated as well. To do this we make use of another helper class called `Schedule`. The reason we move the schedule to an extra class is that the measured schedule, shown in Fig. 4.2b, is stored in a file. Thus, by transferring the schedule to a helper class, like for the class `Lattice`, we keep the number of file operations to a minimum and have to read the file only once per simulation. Finally, we rely on the `Faddeeva`-Package [22] to compute the error function for complex arguments in Eqs. (4.32) and (4.35).

With the base classes described above, we implement the time-dependent KMC algorithm described in Sec. 4.1.3. To generate the needed random numbers we use an instance of the Mersenne Twister 19937 pseudo-random number generator from `C++` Standard Library, i. e. `std::mt19937`. Furthermore, we parallelized the execution such that each run runs in its own thread, using `std::thread`. Finally, we use `boost/filesystem` and `boost/program_options` to conveniently create a directory for the result files and passing command line options to the program.

## 4.4 Result

In this section we present the results we get from the simulation. For the simulation we use the same 1000 different sets of couplings $\{J_{ij}\} = \pm 1$, called instances, as have been used in [12] and published in [15]. We repeat the simulation for each instance 100 times, called runs, count the number of runs where the ground state was reached and determine the success probability of finding the ground state. To compute the correct ground state energy, we use the Spin Glass Server at the university of Cologne [23].

Applying the method described above to the model with strong coupling to the environment, i. e. when

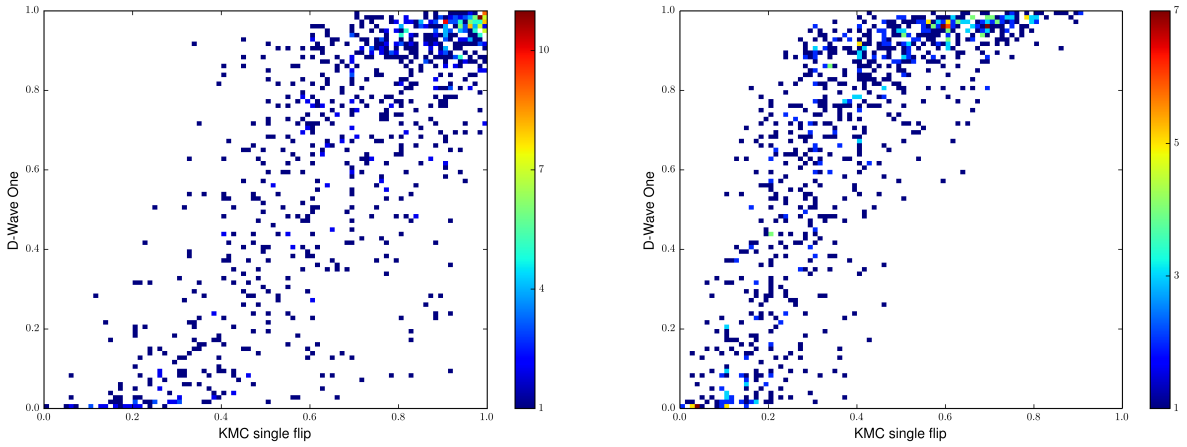


(a) (b)

**Figure 4.4:** Correlation of the probabilities of finding the ground state of 1000 different spin glass instances with $N = 108$ spins for strong coupling to the environment, i. e. $\theta(t) = 0$ between the D-Wave One and (a) the linear and (b) measured annealing schedule from the simulation shown in Fig. 4.3. The color scale indicates the number of instances found in one pixel of the plots.

$\theta(t) = 0$, we get the success probability distribution shown in Fig. 4.3. In both cases, for the linear and measured annealing schedule, we get a unimodal distribution, similar to the classical simulated annealing (SA) in [12]. The analogy to SA becomes more clear when we compare the success probability from the simulation with the one from the experiment on the D-Wave One for each instance individually, which has been done in Fig. 4.4. There we can see a step in the correlation near the peak of the success probability distribution like for SA.

The shift of the peak of the probability distribution can directly be explained by the model. For $\theta(t) = 0$, the only transition rate is given by the flip rate, Eq. (4.32), $\Gamma_{\mathrm{F}}^{l} \propto \Delta^2 = \mathrm{A}^2(t)$. From this follows, that the transition rate for the measured schedule, where $\mathrm{A}(t)$ becomes zero at $t/t_f \approx 0.6$, drops much faster to zero then for the linear schedule, where $\mathrm{A}(t)$ only becomes zero at $t = t_f$. But that also means that the KMC algorithm makes less steps and thus flips less spins for the measured schedule. This is also a result from the simulation, where on average the simulation makes $N_{\mathrm{steps}}^{\mathrm{lin},k_BT=0.1} \approx 180\,000$ steps for the linear but only $N_{\mathrm{steps}}^{\mathrm{meas},k_BT=0.1} \approx 20\,000$ for the measured schedule.

When we increase the temperature we get right the opposite effect. By increasing the temperature, from $k_BT = 0.1$ to $k_BT = 0.3$, the average number of steps increases a lot, $N_{\mathrm{steps}}^{\mathrm{lin},k_BT=0.3} \approx 880\,000$ for the linear and $N_{\mathrm{steps}}^{\mathrm{meas},k_BT=0.3} \approx 120\,000$ for the measured annealing schedule, while at the same time the probability of finding the ground state drops, Fig. 4.5. Here is the case of the measured annealing schedule, Fig. 4.5, of special interest, as its success probability drops basically to zero. But, a closer look at the result shows that the simulation still minimizes the energy, even when it does not find the ground state. By taking the average difference of the energy received from the simulation $E_{\mathrm{sim}}$ and the ground state energy $E_{\mathrm{GS}}$ of the corresponding instance, i. e. $\Delta E^{\mathrm{av}} = \mathrm{average}(E_{\mathrm{sim}} - E_{\mathrm{GS}})$, we find that the average result is with $\Delta E_{\mathrm{meas}}^{\mathrm{av}} = 34.2 \pm 14.9$ about 10% larger than the ground state energy, $E_{\mathrm{GS}} \in [-308, -358]$ for the given instances, but also has a large spread. We interpret this result that, by increasing the temperature, thermal excitations become more important and thus that

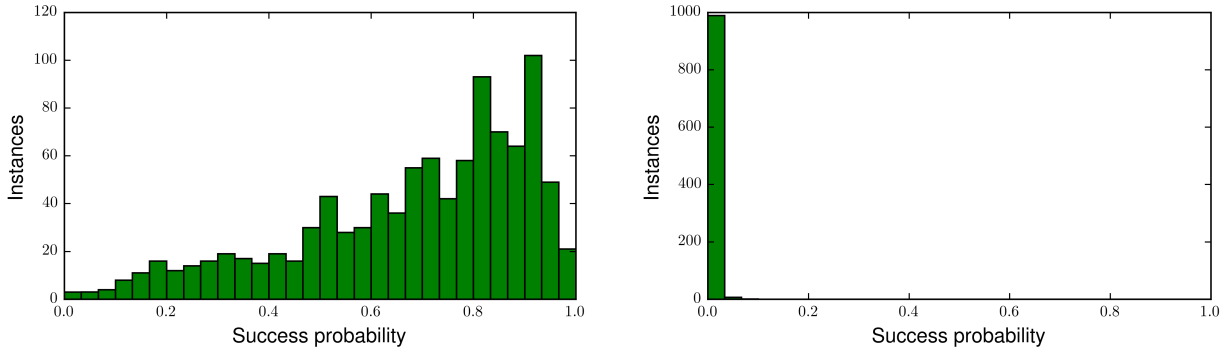


(a) (b)

**Figure 4.5:** Histogram of the probabilities of finding the ground state of 1000 different spin glass instances with $N = 108$ spins for strong coupling to the environment, i. e. $\theta(t) = 0$. For the simulation we use the time-independent KMC, a temperature of $k_B T = 0.3$, and (a) the linear and (b) the measured annealing schedule.

the randomness in the spin configuration rises.

Note, that for the model of strong coupling to the environment, i. e. when $\theta(t) = 0$, the transition rates only change slowly in time. Especially, at $t = 0$ the transition rates have a rather large value constant in energy. Thus it is sufficient to use the time-independent version of the KMC algorithm. This can be confirmed in Fig. 4.6, where the result of the simulation with the same parameters as in Fig. 4.3a but with the time-dependent version of the KMC is shown. The results of both methods correlate strongly, which can be seen in Fig. 4.6b.

For the model of weak coupling, i. e. when $\theta(t) = \pi/2(1 - t/t_f)$, the time-independent KMC can no longer be used. In this case, the single-flip rate $\Gamma_{\mathrm{F}}^{l} \propto \Delta_l^2 \propto \cos\theta^2$ and the double-flip rate $\Gamma_{\mathrm{DF}} \propto M_{lm}^2 \propto \mathrm{B}^2(t)$ are either zero or very small at the beginning of the simulation. Therefore, if the time-independent KMC is used, the first time step becomes extremely large and even exceeds the simulation time $t_f$.

In addition to the change to the time-dependent KMC we now also add the classical annealing, with transition rate Eq. (4.40), at the end of the simulation. Thereby, we choose the classical annealing to start at the time of the last step in the quantum KMC, i. e. at the time of the last transition of the state before the simulation time $t_f$ was reached. In Fig. 4.7 the result of the simulation is shown. There we can see, that, similar to the case of the measured annealing schedule at temperature $k_B T = 0.3$, the simulation fails almost every time. When we again take a look at the average difference of the energy received by the simulation $E_{\mathrm{sim}}$ and the ground state energy $E_{\mathrm{GS}}$ of the corresponding instance, i. e. $\Delta E^{\mathrm{av}} = \mathrm{average}(E_{\mathrm{sim}} - E_{\mathrm{GS}})$, which yields $\Delta E_{\mathrm{lin}}^{\mathrm{av}} = 12.7 \pm 8.4$ for the linear and $\Delta E_{\mathrm{meas}}^{\mathrm{av}} = 8.7 \pm 7$ for the measured annealing schedule, we can once again see that the energy gets minimized, albeit it does not find the ground state. Thus there is too much randomness in the spin configuration.

Moreover, the weak coupling model shows am interesting effect when we increase the temperature. While in the strong coupling model an increase in temperature causes the peak of the success probability distribution to shift to lower probabilities, the weak coupling model shows the opposite effect. Here an increase from $k_B T = 0.1$ to $k_B T = 0.3$ causes the average number of steps to grow by the factor $\approx 3.5$ and also shifts the peak of the success probability to higher probabilities. In Fig. 4.8 the result

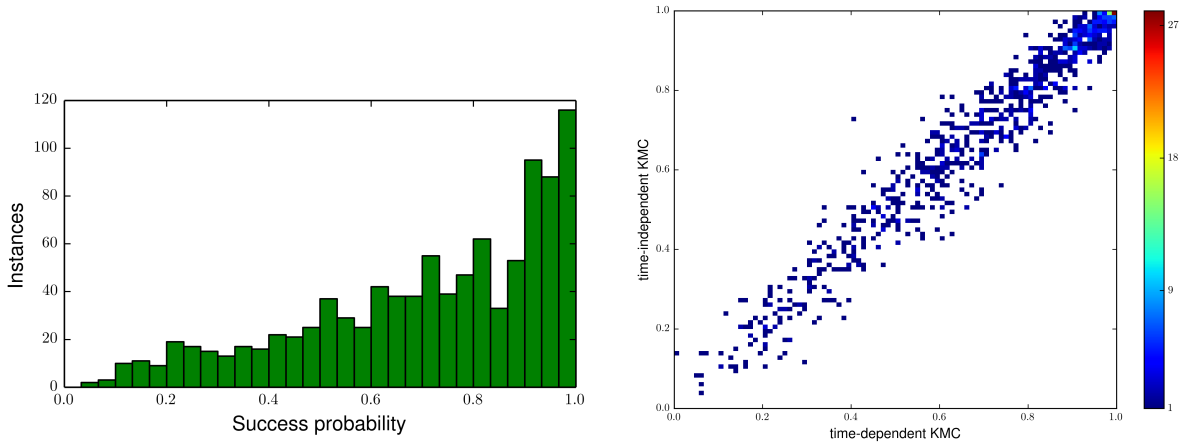


(a) (b)

**Figure 4.6:** (a) Histogram of the probabilities of finding the ground state of 1000 different spin glass instances with $N = 108$ spins for strong coupling to the environment, i. e. $\theta(t) = 0$. For the simulation we use the time-dependent KMC, a temperature of $k_BT = 0.1$, and the linear annealing schedule. (b) Correlation between the time-dependent KMC from (a) and the corresponding time-independent KMC from Fig. 4.3a. Both simulations show a high correlation.

of the simulation with temperature $k_BT = 0.3$ is shown, where especially the result of the measured annealing schedule is of interest as it shows a similar, unimodal result like the strong coupling model at $k_BT = 0.1$.

When we compare the result of this case instance by instance with the result of the D-Wave One, shown in Fig. 4.9a, we see again a step in the correlation like for the weak coupling limit and the SA in [12]. In contrast to this the direct comparison of the weak, at $k_BT = 0.3$, and the strong coupling to the environment model, at $k_BT = 0.1$, shown in Fig. 4.9b, shows a strong correlation. This is quite surprisingly as the number of steps in the weak coupling limit is, with $N_{\text{steps}}^{\text{weak}} \approx 90\,000 + 7000$, where the second number gives the number of steps of the classical annealing, about five times higher than the number of steps in the strong coupling limit. Therefore the energy dependency of the transition rates must be smaller. The reason for this is unknown and needs further investigation.

Finally let us investigate what influence the classical annealing has on the success probability. The result of the simulation with the measured annealing schedule at $k_BT = 0.3$ without classical annealing, Fig. 4.10a, shows again a unimodal distribution with the peak shifted to lower probabilities. The fact that the peak is only shifted can also be seen in its strong correlation to the simulation of the strong coupling model at $k_BT = 0.1$ in Fig. 4.10b. A similar behaviour can be seen for the other cases, e. g. for the linear annealing schedule, but, as the peaks are too far at low probabilities, the effect is less visible. Thus the classical annealing has no qualitative effect on our results.

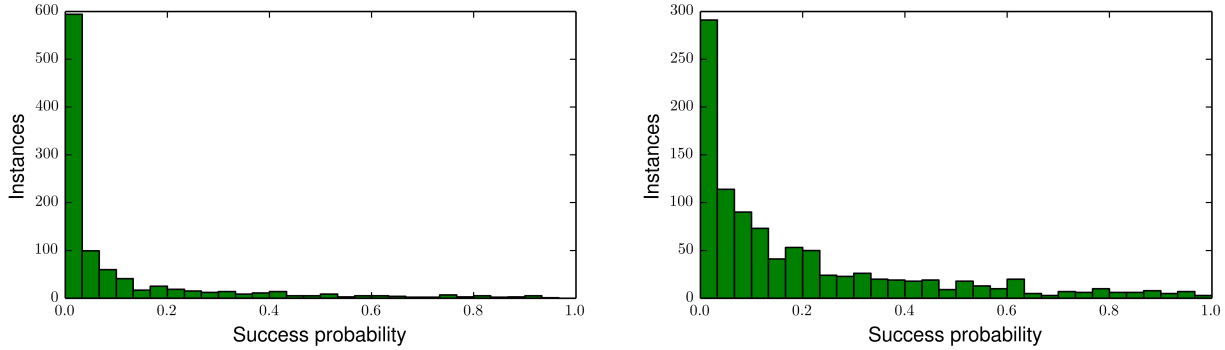


(a) (b)

**Figure 4.7:** Histogram of the probabilities of finding the ground state of 1000 different spin glass instances with $N = 108$ spins for weak coupling to the environment, i. e. $\theta(t) = \pi/2(1 - t/t_f)$. For the simulation we use the time-dependent KMC with classical annealing at the end of the simulation, a temperature of $k_B T = 0.1$, and (a) the linear and (b) the measured annealing schedule.

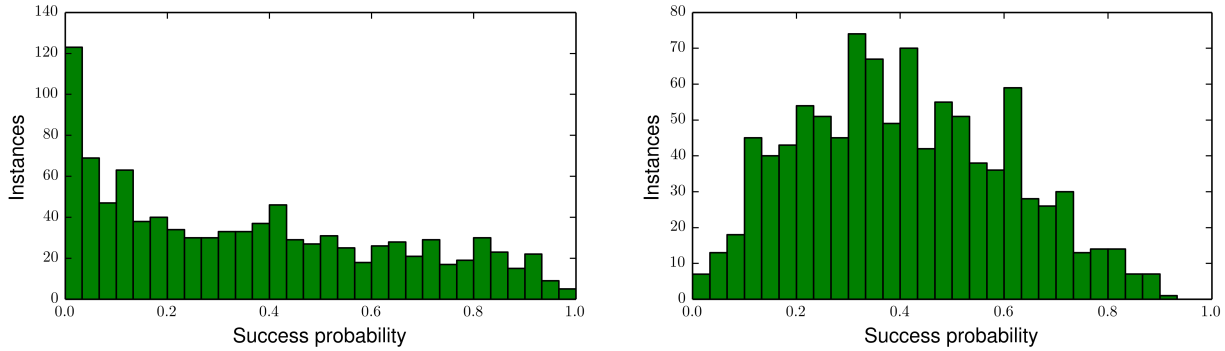


(a) (b)

**Figure 4.8:** Histogram of the probabilities of finding the ground state of 1000 different spin glass instances with $N = 108$ spins for weak coupling to the environment, i. e. $\theta(t) = \pi/2(1 - t/t_f)$. For the simulation we use the time-dependent KMC with classical annealing at the end of the simulation, a temperature of $k_B T = 0.3$, and (a) the linear and (b) the measured annealing schedule.

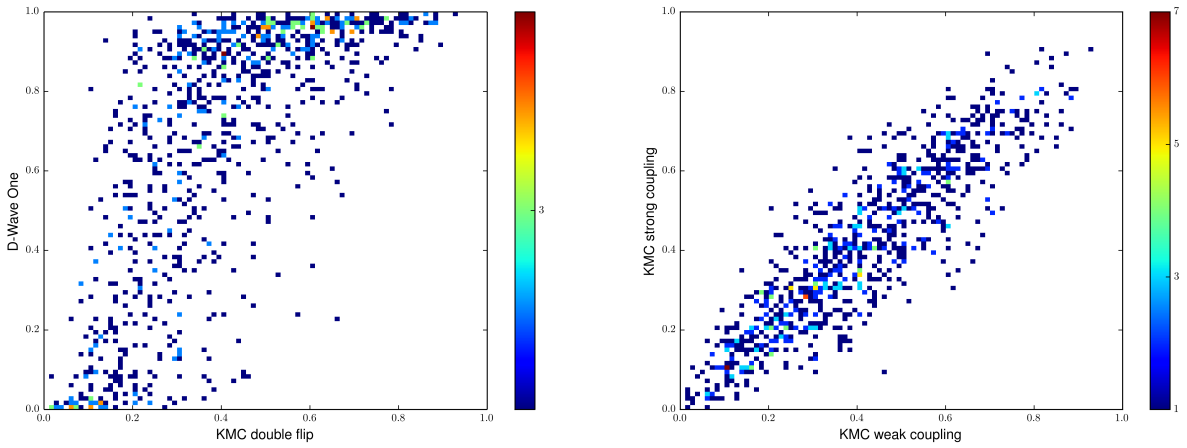


(a) (b)

**Figure 4.9:** Correlation of the probabilities of finding the ground state of 1000 different spin glass instances with $N = 108$ spins between the simulation in the weak coupling limit at temperature $k_BT = 0.3$, from Fig. 4.8b, and (a) the D-Wave One and (b) the simulation in the strong coupling limit at temperature $k_BT = 0.1$, from Fig. 4.3b. The color scale indicates the number of instances found in one pixel of the plots.

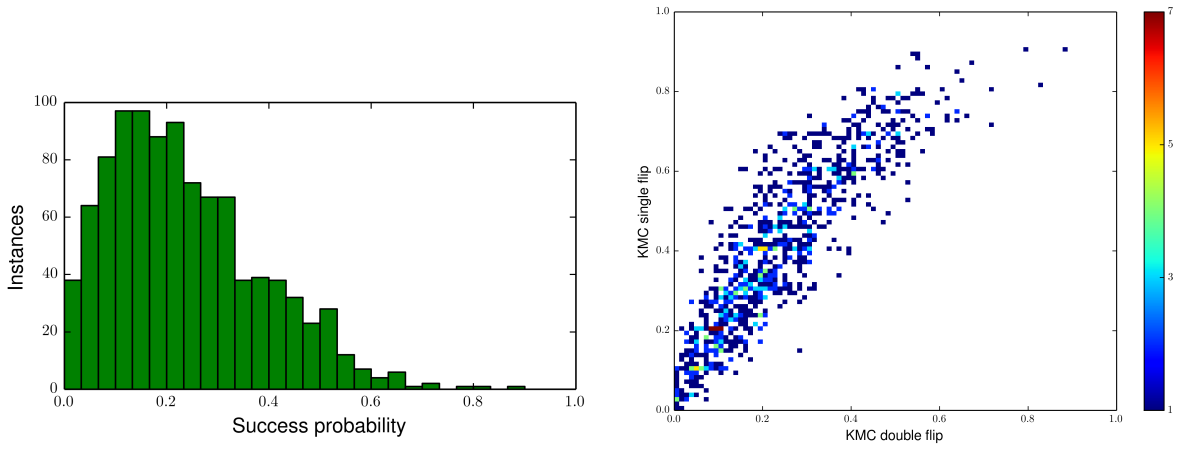


(a) (b)

**Figure 4.10:** (a) Histogram of the probabilities of finding the ground state of 1000 different spin glass instances with $N = 108$ spins for weak coupling to the environment, i. e. $\theta(t) = \pi/2(1-t/t_f)$. For the simulation we use the time-dependent, KMC without classical annealing, at temperature $k_BT = 0.3$, and the measured annealing schedule. (b) Correlation between the result from (a) and the simulation in the strong coupling limit at temperature $k_BT = 0.1$, from Fig. 4.3b. The color scale indicates the number of instances found in one pixel of the plot.

# Chapter 5
# 5 Discussion

We started this work with the motivation to better understand the behaviour of a D-Wave quantum annealer. As for isolated qubits the eigenbasis would change during the adiabatic evolution, we set a focus on the influence of the environment on the choice of the eigenbasis. Therefore we developed a microscopically motivated model in which all required parameters can be taken from experiments already performed on the flux qubits used in the D-Wave One. In our model, the qubit eigenbasis is rotated by an angle $\theta$ towards the eigenbasis in an static environment. We derived its dynamics using lowest-order perturbation theory and investigated the behaviour of the rotation angle $\theta$ over time for a single and two coupled qubits. In both cases we see that the rotation angle behaves differently depending on the state the qubit is in. When the qubit is in the ground state the eigenbasis is given by the original, unrotated basis, while when it is in the excited state the basis starts fully rotated and, at a given time, jumps to the original basis. This jump is problematic as it happens instantaneously and is accompanied with a jump in the qubit energy and thus contradicts the expected adiabatic behaviour.

Furthermore we used a simplified version of the model to simulate its capability of finding the ground state of an Ising spin glass with 108 spins, using the Kinetic Monte Carlo method. In the simulation we investigated the same 1000 random sets of coupling as has been used in [12] and published in [15]. In contrast to our findings from the single and two qubit case, we modeled the rotation angle $\theta$ in the simulation to be either in the original, unrotated basis throughout the simulation or to start in the fully rotated basis and change linear in time to the original basis. Furthermore we considered two models for the annealing parameters $\mathrm{A}(t)$ and $\mathrm{B}(t)$. The first is the linear schedule, where $\mathrm{A}(t)$ decreases and $\mathrm{B}(t)$ increases linearly in time, and the second are measured values from a D-Wave One.

The simulation shows that all considered parameters were able to minimize the energy of the Ising spin glass, although the probability of finding the ground state varied strongly with the choice of parameters. Overall, the success probability of finding the ground state has a unimodal distribution and also shows in the instance by instance comparison strong similarity to the classical simulated annealing algorithm. In addition to this both models for the rotation angle show a high correlation.

In conclusion, the simulation shows that the simplified form of our model reproduces the result of the classical annealing algorithm and thus does not explain the output of the D-Wave One. However, several simplifying assumptions were made which later proved to be too simplistic. In this context, especially the choice of the qubit eigenbasis, i. e. the behavior of the rotation angle $\theta$, is of interest as here our simplifying assumption differ most from the findings in the toy models. Thus, further efforts are needed to better understand its behaviour for larger numbers of qubits. With this we hope to find more realistic models for the rotation angle which can be used in the simulation.

# Bibliography


[1] RichardP. Feynman. Simulating physics with computers. *International Journal of Theoretical Physics*, 21(6-7):467–488, 1982. ISSN 0020-7748. doi: 10.1007/BF02650179. URL http://dx.doi.org/10.1007/BF02650179.
(Cited on page 1.)

[2] P. Shor. Polynomial-time algorithms for prime factorization and discrete logarithms on a quantum computer. *SIAM Journal on Computing*, 26(5):1484–1509, 1997. doi: 10.1137/S0097539795293172. URL http://dx.doi.org/10.1137/S0097539795293172.
(Cited on page 1.)

[3] Edward Farhi, Jeffrey Goldstone, Sam Gutmann, Joshua Lapan, Andrew Lundgren, and Daniel Preda. A quantum adiabatic evolution algorithm applied to random instances of an np-complete problem. *Science*, 292(5516):472–475, 2001. doi: 10.1126/science.1057726. URL http://www.sciencemag.org/content/292/5516/472.abstract.
(Cited on page 1.)

[4] D. Aharonov, W. van Dam, J. Kempe, Z. Landau, S. Lloyd, and O. Regev. Adiabatic quantum computation is equivalent to standard quantum computation. *SIAM Journal on Computing*, 37(1):166–194, 2007. doi: 10.1137/S0097539705447323. URL http://dx.doi.org/10.1137/S0097539705447323.
(Cited on pages 1 and 5.)

[5] P. W. Shor. Fault-tolerant quantum computation. In *Proceedings of the 37th Annual Symposium on Foundations of Computer Science*, FOCS '96, pages 56–, Washington, DC, USA, 1996. IEEE Computer Society. URL http://dl.acm.org/citation.cfm?id=874062.875509.
(Cited on page 1.)

[6] Boris Altshuler, Hari Krovi, and Jérémie Roland. Anderson localization makes adiabatic quantum optimization fail. *Proceedings of the National Academy of Sciences of the United States of America*, 107(28):12446–12450, June 2010. ISSN 1091-6490. URL http://www.ncbi.nlm.nih.gov/pmc/articles/PMC2906561/.
(Cited on page 1.)

[7] D-wave systems homepage. URL http://www.dwavesys.com/our-company/meet-d-wave.
(Cited on page 2.)

[8] Edward Farhi, Jeffrey Goldstone, Sam Gutmann, and Michael Sipser. Quantum computation by adiabatic evolution. 2000. URL http://arxiv.org/abs/quant-ph/0001106v1.
(Cited on page 5.)

[9] R. Harris, J. Johansson, A. Berkley, M. Johnson, T. Lanting, Siyuan Han, P. Bunyk, E. Ladizinsky, T. Oh, I. Perminov, E. Tolkacheva, S. Uchaikin, E. Chapple, C. Enderud, C. Rich, M. Thom,

J. Wang, B. Wilson, and G. Rose. Experimental demonstration of a robust and scalable flux qubit. *Phys. Rev. B*, 81:134510, Apr 2010. doi: 10.1103/PhysRevB.81.134510. URL http://link.aps.org/doi/10.1103/PhysRevB.81.134510.
(Cited on page 7.)

[10] M. H. S. Amin and Dmitri V. Averin. Macroscopic resonant tunneling in the presence of low frequency noise. *Phys. Rev. Lett.*, 100:197001, May 2008. doi: 10.1103/PhysRevLett.100.197001. URL http://link.aps.org/doi/10.1103/PhysRevLett.100.197001.
(Cited on pages 10, 17, 18, 19, 20, and 41.)

[11] T. Lanting, M. H. S. Amin, M. W. Johnson, F. Altomare, A. J. Berkley, S. Gildert, R. Harris, J. Johansson, P. Bunyk, E. Ladizinsky, E. Tolkacheva, and D. V. Averin. Probing high-frequency noise with macroscopic resonant tunneling. *Phys. Rev. B*, 83:180502, May 2011. doi: 10.1103/PhysRevB.83.180502. URL http://link.aps.org/doi/10.1103/PhysRevB.83.180502.
(Cited on pages 12, 13, 19, and 22.)

[12] Sergio Boixo, Troels F. Rønnow, Sergei V. Isakov, Zhihui Wang, David Wecker, Daniel A. Lidar, John M. Martinis, and Matthias Troyer. Evidence for quantum annealing with more than one hundred qubits. *Nat Phys*, 10(3):218–224, March 2014. ISSN 1745-2473. URL http://dx.doi.org/10.1038/nphys2900.
(Cited on pages 13, 14, 22, 29, 35, 48, 49, 51, and 55.)

[13] John A Smolin and Graeme Smith. Classical signature of quantum annealing. *Frontiers in Physics*, 2(52), 2014. ISSN 2296-424X. doi: 10.3389/fphy.2014.00052. URL http://www.frontiersin.org/interdisciplinary_physics/10.3389/fphy.2014.00052/abstract.
(Cited on page 14.)

[14] Seung Woo Shin, Graeme Smith, John A. Smolin, and Umesh Vazirani. How "quantum" is the d-wave machine?, 2014. URL http://arxiv.org/abs/1401.7087.
(Cited on page 14.)

[15] Lei Wang, Troels F. Rønnow, Sergio Boixo, Sergei V. Isakov, Zhihui Wang, David Wecker, Daniel A. Lidar, John M. Martinis, and Matthias Troyer. Comment on: "classical signature of quantum annealing", 2013. URL http://arxiv.org/abs/1305.5837.
(Cited on pages 14, 47, 48, and 55.)

[16] Tameem Albash, Troels F. Rønnow, Matthias Troyer, and Daniel A. Lidar. Reexamining classical and quantum models for the d-wave one processor, 2014. URL http://arxiv.org/abs/1409.3827.
(Cited on page 14.)

[17] Single charge tunneling : Coulomb blockade phenomena in nanostructures; [proceedings of a nato advanced study institute on single charge tunneling, held march 5 - 15, 1 1991, in les houches, france]. NATO ASI series : Series B, Physics ; 294, New York [u.a.], 1992. Plenum Press. ISBN 0-306-44229-9.
(Cited on page 20.)

[18] Christian Karlewski and Michael Marthaler. Time-local master equation connecting the born and markov approximations. *Phys. Rev. B*, 90:104302, Sep 2014. doi: 10.1103/PhysRevB.90.104302.

URL http://link.aps.org/doi/10.1103/PhysRevB.90.104302.
(Cited on page 23.)

[19] A. Prados, J.J. Brey, and B. Sanchez-Rey. A dynamical monte carlo algorithm for master equations with time-dependent transition rates. *Journal of Statistical Physics*, 89(3-4):709–734, 1997. ISSN 0022-4715. doi: 10.1007/BF02765541. URL http://dx.doi.org/10.1007/BF02765541.
(Cited on page 35.)

[20] Troels F. Rønnow and Matthias Troyer. personal communication.
(Cited on page 43.)

[21] Boost (c++ libraries). URL http://www.boost.org.
(Cited on page 47.)

[22] Steven G. Johnson. Faddeeva w function implementation. URL http://ab-initio.mit.edu/Faddeeva.
(Cited on page 48.)

[23] Spin glass server at university of cologne. URL http://www.informatik.uni-koeln.de/spinglass/.
(Cited on page 48.)